Monthly Notices
of the
ROYAL ASTRONOMICAL SOCIETY

MNRAS **507,** 3998–4015 (2021)
Advance Access publication 2021 August 16

https://doi.org/10.1093/mnras/stab2346

An ALMA view of 11 dusty star-forming galaxies at the peak of cosmic star formation history

L. Pantoni,[1,2,3★] M. Massardi,[3] A. Lapi,[1,2,3,4] D. Donevski,[1,4] Q. D'Amato,[3] M. Giulietti,[1,3] F. Pozzi,[5,6] M. Talia ,[5,6] C. Vignali ,[5,6] A. Cimatti,[5,7] L. Silva,[8] A. Bressan[1] and T. Ronconi[1,2,4]

[1]*SISSA, ISAS, Via Bonomea 265, Trieste I-34136, Italy*
[2]*INFN, Sezione di Trieste, via Valerio 2, Trieste I-34127, Italy*
[3]*INAF, Istituto di Radioastronomia, Italian ARC, Via Piero Gobetti 101, I-40129 Bologna, Italy*
[4]*IFPU, Institute for fundamental physics of the Universe, Via Beirut 2, I-34014 Trieste, Italy*
[5]*DIFA, Dipartimento di Fisica e Astronomia, Università degli Studi di Bologna, Via Berti Pichat 6/2, I-40127 Bologna, Italy*
[6]*INAF, Osservatorio di Astrofisica e Scienza dello Spazio di Bologna, Via Gobetti 93/3, I-40129 Bologna, Italy*
[7]*INAF, Osservatorio Astrofisico di Arcetri, Largo E. Fermi, I-50125, Firenze, Italy*
[8]*INAF, Osservatorio Astronomico di Trieste, Via Giambattista Tiepolo, 11, I-34131 Trieste, Italy*

Accepted 2021 August 11. Received 2021 August 9; in original form 2021 June 15

ABSTRACT

We present the ALMA view of 11 main-sequence dusty star-forming galaxies (DSFGs) (sub-)millimetre selected in the Great Observatories Origins Survey South (GOODS-S) field and spectroscopically confirmed to be at the peak of cosmic star formation history ($z \sim 2$). Our study combines the analysis of galaxy spectral energy distribution with ALMA continuum and CO spectral emission by using ALMA Science Archive products at the highest spatial resolution currently available for our sample ($\Delta\theta \lesssim 1$ arcsec). We include galaxy multiband images and photometry (in the optical, radio, and X-rays) to investigate the interlink between dusty, gaseous, and stellar components and the eventual presence of AGN. We use multiband sizes and morphologies to gain an insight on the processes that lead galaxy evolution, e.g. gas condensation, star formation, AGN feedback. The 11 DSFGs are very compact in the (sub-)millimetre (median $r_{\rm ALMA} = 1.15$ kpc), while the optical emission extends to larger radii (median $r_{\rm H}/r_{\rm ALMA} = 2.05$). CO lines reveal the presence of a rotating disc of molecular gas, but we cannot exclude the presence of interactions and/or molecular outflows. Images at higher (spectral and spatial) resolution are needed to disentangle from the possible scenarios. Most of the galaxies are caught in the *compaction* phase, when gas cools and falls into galaxy centre, fuelling the dusty burst of star formation and the growing nucleus. We expect these DSFGs to be the high-z star-forming counterparts of massive quiescent galaxies. Some features of CO emission in three galaxies are suggestive of forthcoming/ongoing AGN feedback, which is thought to trigger the morphological transition from star-forming discs to early-type galaxies.

Key words: galaxies: evolution – galaxies: high-redshift – galaxies: star formation – submillimetre: galaxies.

1 INTRODUCTION

Dusty star-forming galaxies (DSFGs) at high redshift ($z > 1$) have been recognized as a crucial population to characterize massive galaxy evolution across the Universe and constrain the cosmic star formation history (SFH) and stellar mass assembly out to redshift >3 (e.g. Casey, Narayanan & Cooray 2014; Madau & Dickinson 2014). In the last decade, many steps forwards have been taken to obtain a more comprehensive picture of their nature, thanks to the advent of a new generation of (sub-)millimetre/radio telescopes, with increased resolution and sensitivity, e.g. ALMA and JVLA, and to numerous multiwavelength surveys that are essential to characterize DSFG broad-band emission. For example, the Great Observatories Origins Survey South (GOODS-S, Dickinson & GOODS Legacy Team 2001; Giavalisco et al. 2004) field – one of the most studied – was sampled in the X-ray with *Chandra* (Xue et al. 2011; Luo et al. 2017) and *XMM–Newton* (Comastri et al. 2011); in the optical/near-infrared with *HST* (i.e. the HUDF survey, Beckwith et al. 2006) and VLT MUSE (Bacon et al. 2017); in the infrared with *Herschel* (PEP & HerMES, Lutz et al. 2011; Oliver et al. 2012) and *Spitzer* (Labbé et al. 2015); in the (sub-)millimetre with LABOCA (LESS, Weiß et al. 2009), AzTEC/ASTE (Scott et al. 2010) and ALMA (Aravena et al. 2016a, b; Walter et al. 2016; Dunlop et al. 2017); and in the radio band with VLA (Kellermann et al. 2008; Miller et al. 2013; Rujopakarn et al. 2016; Fujimoto et al. 2017). However, we are far away from fully physically characterizing the high-z DSFG population. In particular, we lack a self-consistent explanation of both the mechanisms triggering their intense burst of dust-obscured star formation, with star formation rates (SFRs) $\gtrsim 100$ M$_\odot$ yr^{-1}, and the processes driving their subsequent evolution. In order to reach this goal it is essential, on the one hand, to characterize their integral physical properties (i.e. stellar mass, dust and gas content, gas metallicity, and the activity of the central super massive black hole) by sampling their spectral energy distributions (SEDs; see e.g. Magdis

---

★ E-mail: lpantoni@sissa.it

Published by Oxford University Press on behalf of Royal Astronomical Society

et al. 2012; Béthermin et al. 2014; Małek et al. 2018; Bianchini et al. 2019; Donevski et al. 2020; Dudzevičiūtė et al. 2020). On the other hand, spatially resolved information provides a detailed and precise description of the main baryonic processes occurring inside these galaxies and can be useful to determine their respective importance in driving DSFG evolution. In particular, the latter objective can be reached by exploiting high-resolution imaging of objects that do not appear peculiar in their overall behaviour, so that they could represent the bulk of the $z \sim 2$ DSFG population. The detection of molecular spectral lines and the study of galaxy multiband size and morphology would allow us to investigate galaxy environment and the gas phase properties, such as its kinematics (e.g. Tadaki et al. 2015; Chen et al. 2017; Talia et al. 2018; Hodge et al. 2019). This approach is fundamental to assess the presence of an AGN and characterize its impact on the host galaxy (i.e. AGN *feeding & feedback* cycle; e.g. Bischetti et al. 2021) and, on a statistical basis, on DSFG evolution.

This work is meant to complement the analysis presented in a previous paper from our group (Pantoni et al. 2021) on 11 (sub-)millimetre-selected DSFGs at $z_{\rm spec} \sim 2$ by focusing on the ALMA view of the galaxies. Our 11 DSFGs are located in the GOODS-S field and have an almost complete sampling of their multiwavelength broad-band emission, from the X-rays to the radio band, which was extensively studied in Pantoni et al. (2021). In a nutshell, we modelled the galaxy optical-to-millimetre SED by performing a multicomponent fitting to the available multiwavelength photometry with the Code Investigating GALaxy Emission (CIGALE; Boquien et al. 2019). We combined Bruzual & Charlot (2003) stellar libraries, Lo Faro et al. (2017) double power law (describing stellar attenuation due to dust extinction), and the mid- and far-IR dust emission model by Casey (2012) with new physical motivated prescriptions for dust absorption in the birth molecular clouds of stars. Then, we included in our analysis other information coming from integrated CO spectroscopy and galaxy emission in the X-rays and radio band, providing a self-consistent picture of the ongoing processes concerning galaxy baryonic components, i.e. stars, interstellar medium (ISM) – and its molecular and dusty phases – and central Super Massive Black Hole (SMBH). To this aim, we referred to one possible scenario for galaxy formation and evolution, the so-called *in situ* galaxy-BH co-evolution scenario (see e.g. Mancuso et al. 2016a, b; Shi et al. 2017; Lapi et al. 2018; Pantoni et al. 2019).

In the following, we present the spatially resolved analysis of millimetre and (sub-)millimetre continuum and CO emission lines, as observed with ALMA, in order to derive the size of interstellar dust and CO emission, the molecular gas content, and its kinematics. We complement the ALMA view of the galaxies with resolved multiband information (size and morphology) found in the literature (e.g. van der Wel et al. 2012; Targett et al. 2013; Rujopakarn et al. 2016, 2019; Kaasinen et al. 2020). Comparing galaxy morphology and size in different spectral bands is informative of the processes that are driving the ongoing burst of star formation, the accretion of central SMBH, and its eventual activity, and can tell us if and how the AGN affects the whole host galaxy evolution. The optical rest-frame light samples the stellar component and thus its spatial distribution into galaxy; rest-frame MIR and FIR emission samples the interstellar dust, while the CO emission traces the molecular gas. The relative size of these components provides a hint on their origin, their role in fuelling the star formation, and the central SMBH accretion. The multiband morphology (e.g. isolated or disturbed) is a result of gas condensation and star formation processes occurring inside the galaxies and of eventual interactions with the surrounding ambient and/or galaxy companions (Lacey et al. 2016; Calura et al. 2017; Popping, Somerville & Galametz 2017; Lapi et al. 2018; Davé et al. 2019).

By including in our picture the outcomes of the SED analysis presented in Pantoni et al. (2021), we provide a consistent and physically motivated interpretation of the observations in the broad context of galaxy formation and evolution, which encompasses photometry, spectroscopy, and imaging at high resolution ($\Delta\theta \lesssim 1$ arcsec).

This article is organized as follows. In Section 2, we summarize the main selection criteria used to build our sample of 11 DSFGs at $z \sim 2$ including a brief characterization of the galaxies based on previous results (Pantoni et al. 2021); in Section 3 and Section 4 we analyze the ALMA continuum and spectroscopic emission of the sources, derive dust and molecular gas size and spatial distribution and the total content of molecular gas, and provide a possible description of the gas kinematics from CO lines, when detected. In Section 5, we discuss the main results for the whole sample in the broad context of galaxy formation and evolution. In Section 6, we summarize the outcomes and outline our conclusions. In Appendix A, we include a panchromatic analysis of the individual galaxies evolution.

Throughout this work, we adopt the standard flat ΛCDM cosmology Planck Collaboration VI (2020) with rounded parameter values: matter density $\Omega_{\rm M} = 0.32$, dark energy density $\Omega_\Lambda = 0.63$, baryon density $\Omega_{\rm b} = 0.05$, Hubble constant $H_0 = 100\, h$ km s^{-1} Mpc^{-1} with $h = 0.67$, and mass variance $\sigma_8 = 0.81$ on a scale of 8 h^{-1} Mpc.

2 THE SAMPLE

The sample is constituted by 11 DSFGs observed in the GOODS-S (Dickinson & GOODS Legacy Team 2001; Giavalisco et al. 2004) field and spectroscopically confirmed to be at the peak of cosmic SFH ($z \sim$2). They were selected in the (sub-)millimetre regime requiring the following criteria to be fulfilled for each galaxy: three or more detections in the optical domain ($\lambda_{\rm obs} = 0.3 - 1$ μm); six or more detections in the NIR + MIR bands ($\lambda_{\rm obs} = 1 - 25$ μm); two or more detections in the FIR band ($\lambda_{\rm obs} = 25 - 400$ μm); spectroscopically confirmed redshift in the range of $1.5 < z < 3$; and one or more detections and/or upper limits in the radio and X-ray regimes. For the detailed description of source selection and multiwavelength counterparts association, we refer to Pantoni et al. (2021).

Thanks to the aforementioned selection criteria, in Pantoni et al. (2021) we achieved a complete and accurate sampling of galaxy multiwavelength broad-band emission (from X-rays to radio band) that was essential to derive galaxy integral properties (such as galaxy age, stellar mass, dust and gas content, the presence of an accreting/active central BH) by fitting their SED with CIGALE (Boquien et al. 2019), assuming a Chabrier (2003) initial mass function.

Source IDs are listed in Table 1, along with their spectroscopic redshift, their optical size (i.e. circularized radius $r_{\rm H}$, derived by using the semimajor axis and axes ratio by van der Wel et al. 2012; Rujopakarn et al. 2019), the presence of an AGN (by Luo et al. 2017), and some of their main astrophysical properties, i.e. stellar mass $M_\star$, SFR, and interstellar dust mass $M_{\rm dust}$, already presented in Pantoni et al. (2021). The 11 DSFGs are (almost) main-sequence objects (i.e. staying within its 2σ scatter ∼0.4 dex; see Speagle et al. 2014), with median $M_\star = 6.5 \times 10^{10}$ M$_\odot$ (first quartile 5.7×10^{10} M$_\odot$ and third quartile 9×10^{10} M$_\odot$) and SFR ∼250 M$_\odot$ yr^{-1} (first quartile 90 M$_\odot$ yr^{-1} and third quartile 400 M$_\odot$ yr^{-1}). They are experiencing an intense and dusty burst of star formation (median $L_{\rm IR} \sim 2 \times 10^{12}$ L$_\odot$), with a median duration $\tau_\star \sim 750$ Myr (first quartile 300 Myr and third quartile 900 Myr). Despite their young age, the interstellar

Table 1. Main galaxy properties from literature. In the order: (sub-)millimetre source ID; IAU ID; spectroscopic redshift (z); presence of an AGN by Luo et al. (2017); H_{160} circularized size (r_H) derived from Rujopakarn et al. (2019) for UDF1 (assuming the axes ratio by van der Wel et al. 2012), and computed by Pantoni et al. (2021) from the effective Sérsic half-light semi-axis by van der Wel et al. (2012) for all the other sources; stellar mass ($M_\star$), star formation rate (SFR), and dust mass ($M_{\rm dust}$) by Pantoni et al. (2021).

ID	IAU ID	z	AGN	r_H (kpc)	$M_\star$ (10^{10} M$_\odot$)	SFR (M$_\odot$ yr^{-1})	$M_{\rm dust}$ (10^8 M$_\odot$)
UDF1	J033244.01-274635.2	2.698 ± 0.001^{a}	✓	2.6	8 ± 1	352 ± 18	5.6 ± 0.2
UDF3	J033238.53-274634.6	$2.544^{+0.001}_{-0.002}\,^{a}$	✓	1.6	9 ± 1	519 ± 38	4.0 ± 1.6
UDF5	J033236.94-274726.8	1.759 ± 0.008^{b}	**nd**	2.3	2.4 ± 0.3	85 ± 6	4.6 ± 2.2
UDF8	J033239.74-274611.4	$1.5510^{+0.0014}_{-0.0005}\,^{a}$	✓	5.7	6.5 ± 0.3	100 ± 5	2.4 ± 1.3
UDF10	J033240.73-274749.4	2.086 ± 0.006^{b}	✗	2.0	2.5 ± 0.3	41 ± 5	1.9 ± 1.3
UDF11	J033240.06-274755.5	$1.9962 \pm 0.0014^{c,d}$	✗	4.5	6.4 ± 0.9	241 ± 19	1.46 ± 0.66
UDF13	J033235.07-274647.6	2.497 ± 0.008^{b}	✓	1.2	6.5 ± 1.4	111 ± 17	1.20 ± 0.68
ALESS067.1	J033243.19-275514.3	$2.1212^{+0.0014}_{-0.0005}\,^{a}$	✓	6.5	29 ± 3	485 ± 24	10 ± 4
AzTEC.GS25	J033246.83-275120.9	2.292 ± 0.001^{e}	✓	1.8	8 ± 2	401 ± 20	13.6 ± 8.2
AzTEC.GS21	J033247.59-274452.3	1.910 ± 0.001^{f}	✓	3.7	18 ± 2	360 ± 18	5.8 ± 1.4
AzTEC.GS22	J033212.55-274306.1	1.794 ± 0.005^{g}	**nd**	3.2	5.7 ± 0.5	91 ± 5	14 ± 8

Notes. References for spectroscopic redshifts: [a]This work. [b]Momcheva et al. (2016). [c]Kurk et al. (2013). [d]Dunlop et al. (2017). [e]Popesso et al. (2009). [f] Vanzella et al. (2008). [g]Targett et al. (2013) and reference therein. **AGN** (object classification by Luo et al. 2017): ✓ means that the galaxy has a signature of AGN; ✗ means that the object is classified as a normal star-forming galaxy; and **nd** stands for *not detected*.

Table 2. ALMA continuum observation setting and results. In the order: ID from literature; project code; member observing unit set ID; frequency band ($\nu_{\rm band}$); angular resolution (i.e. restoring beam, $\Delta\theta$); flux density (S_ν); FWHM of the Gaussian fit of the angular size deconvolved from beam (θ_ν); and linear circularized size ($r_{\rm ALMA}$).

ID	Project code	Member ous	$\nu_{\rm band}$ (GHz)	$\Delta\theta = a_{\Delta\theta} \times b_{\Delta\theta}$ (arcsec × arcsec)	S_ν (μJy)	$\theta_\nu = a_\nu \times b_\nu$ (arcsec × arcsec)	$r_{\rm ALMA}$ (kpc)
UDF1	2017.1.00001.S	A001/X1288/X4c3	B7 (335.50−351.48)	0.10×0.09	2900 ± 300	$0.123 \pm 0.006 \times 0.103 \pm 0.005$	0.46
UDF3	2017.1.00001.S	A001/X1288/X4c7	B7 (335.50−351.48)	0.08×0.07	1600 ± 200	$0.203 \pm 0.014 \times 0.111 \pm 0.009$	0.62
UDF5	2012.1.00173.S	A002/X5a9a13/X7e0	B6 (211.21−231.20)	0.62×0.52	311 ± 49^{D}	0.62×0.52^{sb}	<2.5
UDF8	2012.1.00173.S	A002/X5a9a13/X7e0	B6 (211.21−231.20)	0.62×0.52	208 ± 46^{D}	$1.42 \pm 0.35 \times 0.66 \pm 0.19$	4.1
UDF10	2012.1.00173.S	A002/X5a9a13/X7e0	B6 (211.21−231.20)	0.62×0.52	184 ± 46^{D}	0.62×0.52^{sb}	<2.5
UDF11	2012.1.00173.S	A002/X5a9a13/X7e0	B6 (211.21−231.20)	0.62×0.52	186 ± 46^{D}	$1.02 \pm 0.28 \times 0.61 \pm 0.21$	3.4
UDF13	2015.1.01074.S^{A}	A001/X2d8/Xfd	B7 (335.50−351.48)	0.17×0.15	910 ± 170	0.17×0.15^{sb}	<0.65
ALESS067.1	2012.1.00307.S	A002/X7d1738/X103	B7 (336.00−351.98)	0.14×0.12	4500 ± 400	$0.35 \pm 0.05 \times 0.18 \pm 0.03$	1.1
AzTEC.GS25	2012.1.00983.S	A002/X7d1738/X169	B7 (336.00−351.98)	0.20×0.16	5900 ± 500	$0.38 \pm 0.03 \times 0.22 \pm 0.02$	1.2
AzTEC.GS21	2015.1.00098.S^{A}	A001/X2fe/Xaea	B6 (244.13−262.99)	0.18×0.16	954 ± 74	0.18×0.16^{sb}	<0.7
AzTEC.GS22	2017.1.01347.S	A001/X12a3/X80e	B9 (662.53−685.56)	0.49×0.33	6400 ± 880	0.49×0.33^{sb}	<1.7

Note. For unresolved sources labelled with ^{sb} the synthesized beam size is reported and treated as *upper limits* to the actual source size. ALMA observations labelled with the apex ^{A} have been re-imaged in the context of ARI-L project (https://almascience.eso.org/alma-data/aril; see also Massardi et al. 2021). Flux densities labelled with the apex ^{D} are taken from Dunlop et al. (2017).

dust content is high ($M_{\rm dust} > 10^8$ M$_\odot$) and possibly due to a very rapid enrichment of the ISM (on typical time-scales of 10^7-10^8 yr). The gas mass (i.e. median $M_{\rm gas} \sim 4 \times 10^{10}$ M$_\odot$, derived from dust continuum), which fuels the dusty star formation, will be rapidly depleted over a median time-scale $\tau_{\rm depl} \sim 200$ Myr. Nine objects out of 11 have an X-ray luminous ($L_{2-10\,\rm keV} \gtrsim 10^{42}$ erg s^{-1}) counterpart in the *Chandra* $\simeq 7$ Ms catalogue by Luo et al. (2017) and two of them (UDF1 and UDF8) are clearly dominated in the X-rays by the active nucleus emission ($L_{2-10\,\rm keV} \gtrsim 10^{43}-10^{44}$ erg s^{-1}). Radio luminosities are consistent with the emission coming from galaxy star formation, suggesting that the AGN should be radio silent or quiet.

3 CONTINUUM EMISSION

Continuum (sub-)millimetre light of $z \sim 2$ star-forming galaxies traces the thermal emission coming from interstellar dust grains that are heated by newly formed stars (e.g. Draine 2003). The size and the spatial distribution of dust thermal emission are essential to locate and characterize galaxy dust-obscured star formation that in high-z DSFGs occurs in the form of intense bursts (typical SFRs are of the order of 100−1000 M$_\odot$ yr^{-1}, see e.g. Casey et al. 2014).

We analyze the public ALMA archival maps containing our 11 DSFGs and we select the ones that have the best spatial resolution ($\Delta\theta \lesssim 1$ arcsec) in the wavelength range $\lambda_{\rm obs} \sim 500\mu$m to 3 mm (corresponding to the frequency range $\nu_{\rm obs} \sim 100-600$ GHz). Almost all of the best spatially resolved continuum maps are in ALMA B6 and B7 that, indeed, constitute a very good compromise between spatial resolution and the sampled wavelength. This allows us to provide the most homogeneous information on dust continuum emission. Just for AzTEC.GS22 the image at the best spatial resolution is in B9.

In Table 2, we list the continuum flux densities (S_ν) and sizes (θ_ν) of our sources. We estimate the flux density errors as:

$$eS_\nu = \sqrt{({\rm rms})^2 + (0.1 \times S_\nu)^2} \qquad (1)$$

that is the quadratic sum of the ALMA continuum map rms and a conservative estimation of flux calibration accuracy, i.e. ∼10 per cent for the ALMA bands of our interest: B6, B7, and B9.

We measure the source sizes performing a 2D Gaussian fit of the source emission on the ALMA map by using the task *imfit* embedded in the CASA viewer (CASA release 5.4.0-70). Some of the detections (6 out of 11) are not resolved in the corresponding ALMA map: in such a case, we indicate the synthesized beam size (labelled with the apex *sb*) that provides an upper limit on the source size. The level of

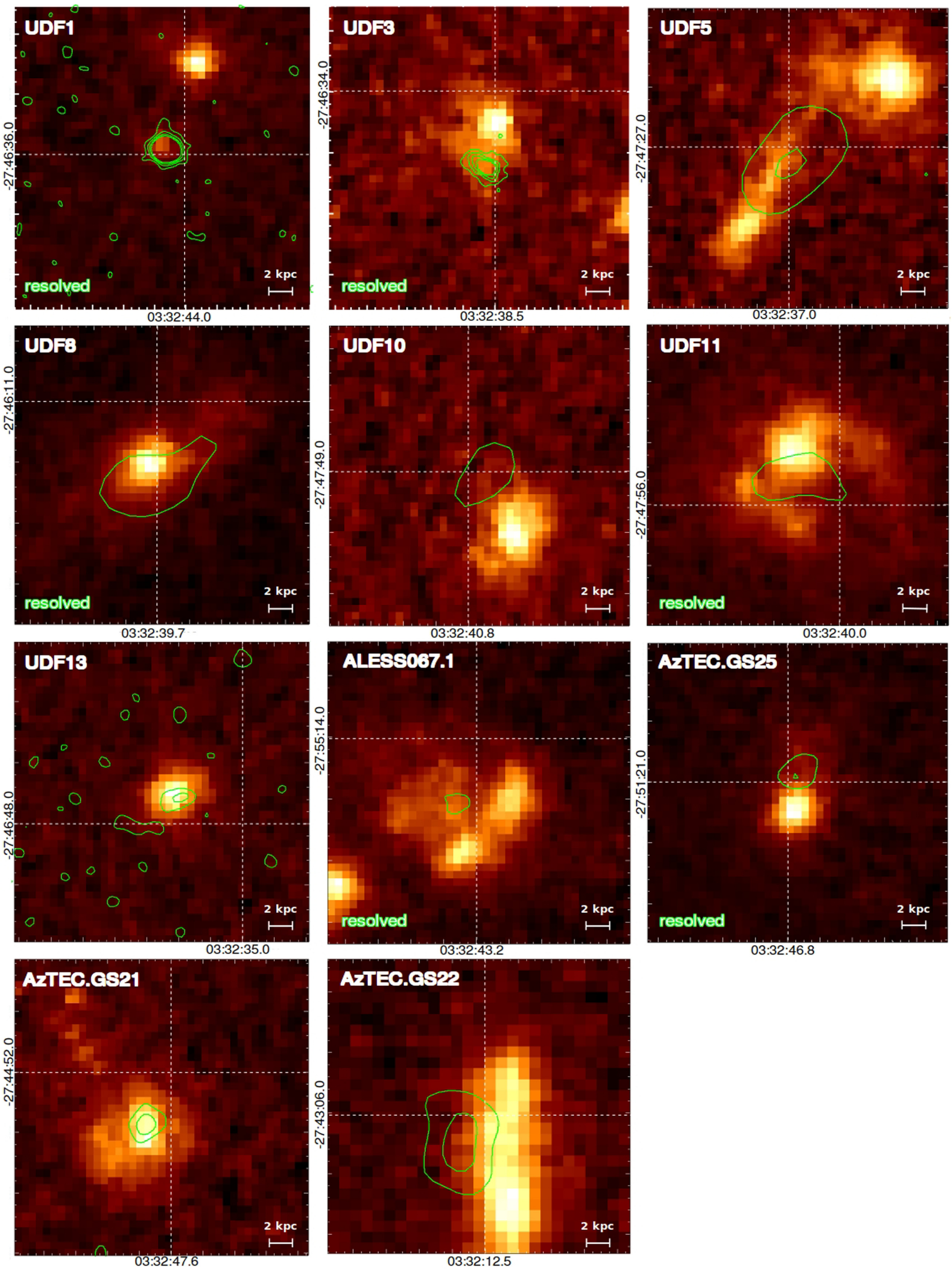

Figure 1. Postage stamps of 2.5 arcsec × 2.5 arcsec. ALMA continuum contours at [1, 2, 3, 4] × 2.5σ (green solid lines) are overlaid on F160W *HST*/WFC3 images (corrected for astrometry). Resolved ALMA sources are labelled as such in the bottom left corner of the panel. In the *x*-axis and *y*-axis, we show the right ascension (RA) in h:m:s and the declination (DEC) in deg:arcmin:arcsec, respectively, for a reference point on the map.

Table 3. ALMA observed CO emission. In the order: ID from literature; project code; member ous ID; velocity resolution (Δv); angular resolution (i.e. restoring beam, $\Delta\theta$); upper level of the CO transition ($J^{\rm up}$); FWHM; CO line intensity ($I_{\rm CO}$); CO angular size (θ_ν); and CO linear circularized size ($r_{\rm CO}$). Quantities preceded with a '<' are *upper limits*.

ID	Project code	Member ous	Δv (km s^{-1})	$\Delta\theta = a_\theta \times b_\theta$ (arcsec × arcsec)	$J^{\rm up}$	$\nu_{\rm obs}$ (GHz)	FWHM (km s^{-1})	$I_{\rm CO}$ (mJy km s^{-1})	θ_ν (arcsec)	$r_{\rm CO}$ (kpc)
UDF1	2017.1.00270.S	A001/X1288/X484	0.85	0.662 × 0.440	3	93.5	170	79.9 ± 7.4	<0.812	<3.3
UDF3	2016.1.00324.L	A001/X87c/X20a	59.4	1.34 × 1.171	3	97.6	190; 390	492 ± 28	0.326	1.35
UDF8	2016.1.00324.L	A001/X87c/X20e	64.1	2.002 × 1.648	2	90.4	148; 379	378 ± 25	0.800	3.45
ALESS067.1	2016.1.00564.S	A001/X879/Xd9	21.2	2.004 × 1.286	3	110.8	115; 314	774 ± 120	0.842	3.6
	2019.2.00246.S	A001/X14c3/Xaf4	21.0	8.330 × 4.363	6	221.6	45	620 ± 70	<3	<26

noise did not allow us to extract the sizes from a fit in the visibility domains.

We derive the linear circularized size of galaxy (sub-)millimetre emission by using the following expression:

$$r_{\rm circ}(\nu)\,[\rm kpc] = \frac{a}{2}\,[\rm arcsec]\,\sqrt{\frac{b}{a}}\;c\;\left[\rm kpc\,arcsec^{-1}\right], \qquad (2)$$

where a and b are the major and minor projected axes; c is the angular-to-linear conversion factor, which depends on redshift and cosmology (see table 12 in Pantoni et al. 2021); and a and b are listed in Table 2 ($\theta_\nu = a_\nu \times b_\nu$). The resulting circularized ALMA sizes ($r_{\rm circ}^{\rm ALMA}$, in kpc) are listed in Table 2. When the source is not (entirely) resolved, we indicate just an upper limit on its size (labelled with the symbol '<'), given by the circularized synthesized beam in kpc.

In Fig. 1, we show the ALMA continuum contours (at [1, 2, 3, 4] $\times\, 2.5\sigma$) overlapping the *HST* (H_{160}) image of the galaxies. Due to the low spatial resolution of *Chandra* X-ray map (Luo et al. 2017), we do not show galaxy X-ray emission on the *HST* maps. We just note that the peak of X-ray emission overlaps both the optical and (sub-)millimetre galaxy counterparts. We corrected the *HST* images astrometry using the position of *Gaia* sources (Gaia Collaboration 2016) that are located in the same field of our DSFGs, finding a mean error of $\sim[+2, -10] \times 10^{-5}$ degrees ($\Delta_{\rm RA} \sim 70$ mas, $\Delta_{\rm DEC} \sim -360$ mas), in agreement with the astrometric error between VLA and *HST* images shown by Rujopakarn et al. (2016), i.e. $\Delta_{\rm RA} = +80 \pm 110$ mas, $\Delta_{\rm DEC} = -260 \pm 130$ mas (see also e.g. Dunlop et al. 2017; Elbaz et al. 2018). The astrometric correction on AzTEC.GS22 *HST* H_{160} image is of $\sim[+15, +5] \times 10^{-5}$ degrees, while we do not apply any correction on AzTEC.GS25 optical coordinates. After the correction, the bulks of the stellar and dust emission coincide within the uncertainties of the astrometric correction (~100 mas) and the beam resolution for most of the galaxies. An eventual remaining shift tells us that the peaks of optical and (sub-)millimetre emission are not exactly coincident due to dust obscuration of stellar light.

4 SPECTROSCOPIC EMISSION

CO transitions can be used to trace the molecular gas phase inside the galaxy and derive its mass, density, and kinetic temperature (e.g. Yang et al. 2017; Joblin et al. 2018; Boogaard et al. 2020). A CO spectral line energy distribution (SLED) peaking at $J > 3$ is typically considered an evidence of shocks and/or nuclear activity, originating from the so-called X-ray dominated regions (see Vallini et al. 2019), while the low-J lines are more commonly associated to star formation (e.g. Pozzi et al. 2017; Mingozzi et al. 2018; Carniani et al. 2019), originating in the Photo-dissociation regions (see Hollenbach & Tielens 1999). Therefore, CO lines can be used to characterize both the ongoing star-forming burst (such as the SFR, see e.g. Bayet et al. 2009) and the impact of the activity of the central SMBH on the host galaxy (Cicone et al. 2014), giving some hints, in particular, on the possible connection between high-z sub-millimetre galaxies (SMGs) and AGN hosts (e.g. Sharon et al. 2016), even if the CO SLED is not entirely sampled.

In the following, we present the five CO $J > 1$ line detections that we found for UDF1, UDF3, UDF8, and ALESS067.1 in the ALMA archive. Images native spectral resolution in most cases was too small to allow the CO line profile to be clearly detected. In such cases, we perform a rebin (using the CASA task *imrebin*[1]) of the line channels. It consents to reduce the noise and boost the source signal by averaging among consecutive channels. We perform a ×15 rebin on UDF1 ALMA data cube and a ×5 rebin on ALESS067.1 ALMA (project code 2016.1.00564.S) data cube. We use instead data cubes of UDF3, UDF8, and ALESS067.1 ALMA (project code: 2019.2.00246.S) as available in the archive with clean spectral resolution as indicated in Table 3. In Figs 2 and 3, we show the observed spectral line profiles with their best Gaussian fits and the maps of spectral line distribution momenta (0, 1, and 2). CO intensity maps are overlapped by dust continuum contours. The angular and linear circularized sizes (θ_ν and $r_{\rm CO}$) are listed in Table 3. Since they all appear unresolved to a 2D Gaussian fit, we provide an upper limit on UDF1 CO emission size, given by the synthesized beam; a measure of UDF3, UDF8, and ALESS067.1 CO emission equal to the angular distance between the peaks of the two spectral line components. We perform the conversion from angular to linear-size exploiting equation (2). Then, we measure CO line intensity on mom0 maps and we list the corresponding values in Table 3.

In Table 3, we also list the CO transition observed for each source and the central observed frequency $\nu_{\rm obs}$ that we use to compute the source redshift z (Table 1). We note that most of the lines [CO(3 − 2) for UDF3 and ALESS067.1; CO(2 − 1) for UDF8; see Figs 2 and 3] are characterized by an asymmetric double-peaked CO line profile, which could suggest that we are observing a tilted disc of rotating molecular gas or a molecular outflow produced by the central engine. Both the explanations are consistent with velocity maps (mom1), which are characterized by null central line (i.e. e.g. the rotation axis), and velocity dispersion maps (mom2), which are peaked along the same line. However, the width of the large components does not exceed 400 km s^{-1}, favouring the first scenario. Merging events seem to be less probable, given the undisturbed appearance of the velocity dispersion on the mom2 maps. UDF1 CO line profile is very narrow [full width at half-maximum (FWHM) ~ 170 km s^{-1}] and shows just a peak: it means that the galaxy cold gas component is actually not rotating or that we are looking at the galaxy *face-on*. The latter interpretation is actually consistent with the velocity dispersion map that is peaked in the centre. These evidences are confirmed also by the velocity range spanned by the CO component in the velocity maps: while for UDF3, UDF8, and ALESS067.1, the CO emission

---

[1] In CASA, *imrebin* performs an average over the binned quantities, in our cases the spectral channels.

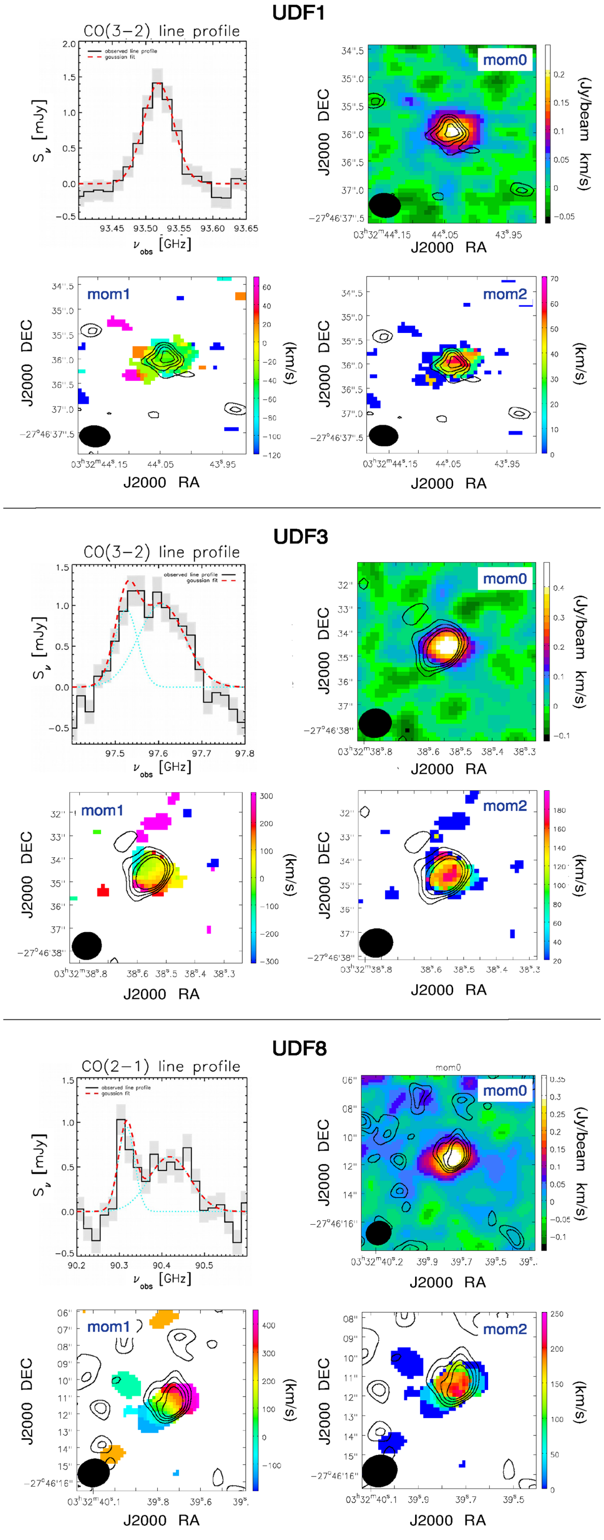

Figure 2. CO lines and spectral analysis for UDF1, UDF3, and UDF8 (from top to bottom). The panels show the observed spectral line profile (black solid line), the corresponding uncertainties on flux density (grey shaded area), and the (total) best Gaussian fit (dashed red line; in case of double-peaked profile, the two components are in cyan); the maps of the spectral line distribution momenta (mom0, mom1, and mom2) overlapped by the continuum contours at [2, 3, 4, 5] × σ detected at the same frequency (ALMA B3). Black filled ellipse in the bottom left corners indicates the beam size.

reaches velocities of the order of a few hundreds $\mathrm{km\,s^{-1}}$, and the CO velocity in UDF1 does not exceed 60 $\mathrm{km\,s^{-1}}$, resembling the intrinsic chaotic motion of the cold gas phase.

Finally, we focus on the case of ALESS067.1 that has two CO lines detected ($J = 3$, $J = 6$; Table 3). The velocity map of ALESS067.1 CO (3-2) (mom1; Fig. 3) does not show a clear null line, while the velocity dispersion map (mom2; Fig. 3) peaks in the centre and shows a tail towards the left upper corner. More likely this could be an indication of an early AGN-driven molecular outflow or an evidence of interactions (e.g. Chen et al. 2017, Calistro Rivera et al. 2018; I note that Targett et al. 2013 claim that ALESS067.1 is actually the central dominant galaxy of a multiple system). However, in the latter scenario we expect the momenta to be much more disturbed. In case we are actually observing an AGN-driven outflow, we do not expect it to significantly affect the galaxy properties and its star formation activity at the moment, since the line FWHM is $<500\mathrm{km\,s^{-1}}$. CO (6-5) maps are both null in the centre, while mom1 map shows a peak to the right upper corner, peaking at 80 $\mathrm{km\,s^{-1}}$. This could trace either the warm star formation of the galaxy or the central engine activity. The low spatial resolution of the image does not allow to spatially compare the size of the two spectral emission, neither to understand the origin of the $J = 6$ line (a nuclear origin implies a very compact size of the CO emission, while a stellar one implies a more extended distribution). We need imaging at higher spatial resolution and sensitivity to definitively disentangle the diverse scenarios. Further details on ALESS067.1 CO spectral line emission along with a possible interpretation in the context of galaxy-BH co-evolution are described in Appendix A8.

4.1 Molecular gas mass

In the following, we exploit the CO line intensity to derive the molecular hydrogen mass content of UDF1, UDF3, UDF8, and ALESS067.1.

We derive CO line luminosity using the following conversion by Solomon et al. (1997):

$$L'_{\mathrm{CO}}\,[\mathrm{K\,km\,s^{-1}\,pc}] = 3.27\times10^{7}\, I_{\mathrm{CO}}\, \nu_{\mathrm{obs}}^{-2}\, d_{\mathrm{L}}^{2}\,(1+z)^{-3}, \tag{3}$$

where I_{CO} is measured in Jy km $\mathrm{s^{-1}}$; ν_{obs} is the observed central frequency of the line (measured in GHz), and z is the corresponding redshift. The luminosity distance d_{L} in Mpc depends on redshift and cosmology (they are listed in Pantoni et al. 2021, their table 6, first column). In Table 4, we list line luminosities. We compute the associated uncertainties by using error propagation theory.

We convert CO $J > 1$ luminosity into the equivalent ground-state luminosity $L'_{\mathrm{CO(1-0)}}$ by using the relation:

$$L'_{\mathrm{CO(1-0)}} = \frac{L'_{\mathrm{CO(J-[J-1])}}}{r_{\mathrm{J1}}} \tag{4}$$

and assuming the CO excitation ladder by Daddi et al. (2015), i.e. $r_{31} = 0.42 \pm 0.07$ and $r_{21} = 0.76 \pm 0.09$.

We derive the molecular hydrogen mass by using the relation:

$$M_{\mathrm{H_2}}[\mathrm{M_\odot}] = \alpha_{\mathrm{CO}}\, L'_{\mathrm{CO(1-0)}}, \tag{5}$$

where α_{CO} is the CO conversion factor in units of $\mathrm{M_\odot}$ [K km $\mathrm{s^{-1}}$ $\mathrm{pc^{2}}]^{-1}$. We assume an $\alpha_{\mathrm{CO}} = 3.6\ \mathrm{M_\odot}$ [K km $\mathrm{s^{-1}}$ $\mathrm{pc^{2}}]^{-1}$ (e.g. Daddi et al. 2015; Decarli et al. 2016b). The resulting molecular hydrogen masses are listed in Table 4. Uncertainties are computed with errors propagation theory.

We note that ALESS067.1 H_2 content ($\mathrm{M}_{H_2} \sim 1.7\times10^{11}\ \mathrm{M_\odot}$; see Table 4) is consistent with the molecular hydrogen mass derived from

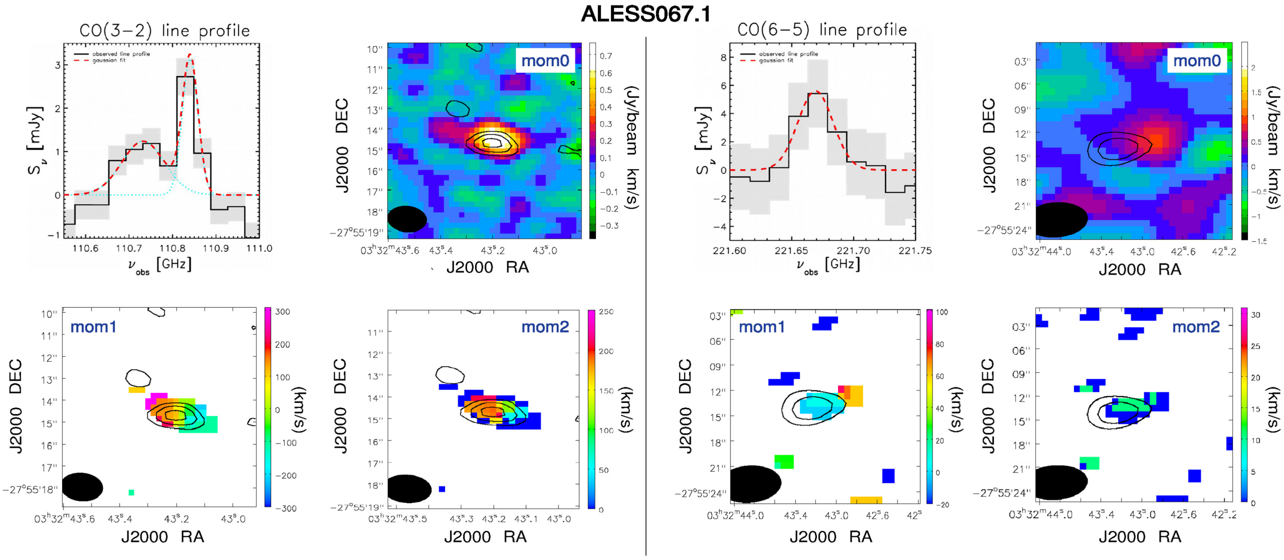

Figure 3. ALESS067.1 CO lines, i.e. $J = 3$ and $J = 6$, in the order. The panels show the observed spectral line profile (black solid line), the corresponding uncertainties on flux density (grey shaded area), and the (total) best Gaussian fit (dashed red line; in case of double-peaked profile, the two components are in cyan); the maps of the spectral line distribution momenta (mom0, mom1, and mom2) overlapped by the continuum contours at [2, 3, 4, 5] × σ detected at the same frequency (ALMA B3 and ALMA B6, respectively). Black filled ellipse in the bottom left corners indicates the beam size.

Table 4. CO analysis: L_{CO} and M_{H_2} for UDF1, UDF3, UDF8, and ALESS067.1 by assuming an $\alpha_{CO} = 3.6$ K km pc^2 s^{-1} M$_\odot^{-1}$.

ID	z_{CO}	J^{up}	L_{CO} (10^8 K km s^{-1} pc^2)	M_{H_2} (10^{10} M$_\odot$)
UDF1	2.698	3	31 ± 3	2.6 ± 0.7
UDF3	2.543	3	170 ± 10	15 ± 3
UDF8	1.5490	2	122 ± 9	5.8 ± 1.1
ALESS067.1	2.1212	3	196 ± 31	16.8 ± 5.4
	2.1212	6	123 ± 45	–

Note. H_2 mass of ALESS067.1 is calculated by exploiting the transition with lower J^{up}.

the CO (1-0) line luminosity measured with the Australian Telescope Compact Array by Huynh et al. (2017), i.e. $L'_{CO(1-0)} = (9.9 \pm 1.8)^{10}$ K km s^{-1} pc^2, and assuming an $\alpha_{CO} = 1.8$ M$_\odot$ [K km s^{-1} pc^2]$^{-1}$ (i.e. $M_{H_2} \sim 1.8 \times 10^{11}$ M$_\odot$; see Chen et al. 2017). The latter conversion factor is often thought to be preferable for compact SMGs (e.g. Carilli & Walter 2013; Chen et al. 2017; Elbaz et al. 2018). Calistro Rivera et al. (2018) found an even smaller CO-to-H$_2$ conversion factor, i.e. $\alpha_{CO} = 1.1^{+0.8}_{-0.7}$ M$_\odot$ [K km s^{-1} pc^2]$^{-1}$, that gives for ALESS067.1 a moleculat hydrogen mass of $(1.0 \pm 0.2) \times 10^{11}$ $M_\odot$. However, due to the large uncertainties on α_{CO}, we do not favour one or the other value and we suggest just to rescale the resulting molecular gas in Table 4 by a factor of 1.8/3.6 = 0.5. The presence of the direct measurement of the CO (1-0) line luminosity for ALESS067.1 by Huynh et al. (2017) allows us to compute r_{31} and r_{61}. We calculate a line luminosity ratio of $r_{31} = L'_{CO(3-2)}/L'_{CO(1-0)} = 0.20 \pm 0.07$ and $r_{61} = L'_{CO(6-5)}/L'_{CO(1-0)} = 0.12 \pm 0.07$. We note that the r_{31} we obtain is smaller than the one measured by Daddi et al. (2015), indicating a more excited CO SLED for ALESS067.1 if compared to the normal (near-IR selected BzK) star-forming disc galaxies at $z = 1.5$ studied by Daddi et al. (2015). Typical values of r_{61} are $\gtrsim 0.2$ for SMGs and even higher for Quasi-Stellar Objects (QSOs) (e.g. Bothwell et al. 2013; Carilli & Walter 2013; Daddi et al. 2015, extrapolations from the latter two). The slightly lower value we find is probably due to sensitivity limit that makes us miss the outskirts of the CO emission, coupled with low resolution that causes the flux to be distributed on a larger image area, while for high-J it is probably mostly concentrated in the central region.

5 DISCUSSION

In this section, we combine our broad-band spatially resolved and spectral analyses with the results obtained from galaxy SED fitting by Pantoni et al. (2021) and additional information collected from literature and multiwavelength images from public catalogues, in order to include the whole sample in a broad context of galaxy formation and evolution.

In Tables 5 and 6, we list the global astrophysical properties of the individual 11 DSFGs in our sample, while in Table 7 we show their median values, with the corresponding first and third quartiles. For reference, we compare the outcomes with a well-studied $z \sim 2$ DSFG (i.e. UDF2) that is not included in our sample but presents a similar multiband sampling of its SED and the same multiwavelength spatially resolved and spectral information (see e.g. Boogaard et al. 2019; Rujopakarn et al. 2019; Kaasinen et al. 2020).

In Table 6, we compute the ratio between the optical (H_{160}) circularized radius and the ALMA size, i.e. r_H/r_{ALMA}. We note that the optical size is typically equal or more extended than the (sub-)millimetre one. This trend is actually observed in many recent works on high-z SMGs (e.g. Barro et al. 2013, 2016a, b; Ikarashi et al. 2015; Simpson et al. 2015; Massardi et al. 2018; Talia et al. 2018; Tadaki et al. 2020), and predicted by some theoretical models describing massive galaxy evolution, focusing in particular on the star-forming progenitors of $z < 1$ early-type galaxies (ETGs). In Fig. 4, we show the size–mass relation as it is predicted in the theoretical scenario by Lapi et al. (2018) in terms of two typical radii: the stability radius to gas fragmentation R_Q (∼ a few kpc for ETG star-forming progenitors at $z > 1$) that is derived from the Toomre stability criterion (see Toomre 1964; Lapi et al. 2018, their equations 9 and 10); the rotational radius R_{rot} (∼1 kpc for ETG star-forming progenitors at $z > 1$), for which the rotational

Table 5. Integral properties of the 11 DSFGs in our sample by Pantoni et al. (2021). We list (in the order): galaxy ID; spectroscopic redshift (references in Table 1); stellar mass ($M_\odot$); star formation rate (SFR); burst age ($\tau_\star$); IR luminosity ($L_{\rm IR}$); AGN fraction in the IR ($f_{\rm AGN}$); dust mass ($M_{\rm dust}$); gas mass ($M_{\rm gas}$); gas depletion time-scale ($\tau_{\rm depl}$); 2–10 keV luminosity (L_X); X-ray dominant component (class X); and presence of an AGN (AGN) by Luo et al. (2017).

ID	$z_{\rm spec}$	$M_\star$ (10^{10} $M_\odot$)	SFR ($M_\odot$ yr^{-1})	$\tau_\star$ (Myr)	$L_{\rm IR}$ (10^{12} $L_\odot$)	$f_{\rm AGN}{}^{(1)}$ (%)	$M_{\rm dust}{}^{(2)}$ (10^8 $M_\odot$)	$M_{\rm gas}{}^{(3)}$ (10^{10} $M_\odot$)	$\tau_{\rm depl}$ (Myr)	L_X (10^{42} erg s^{-1})	Class X	AGN
UDF1	2.698	8 ± 1	352 ± 18	334 ± 58	3.5 ± 0.2	6	5.6 ± 0.2	3^{+3}_{-1}	85	40.2	AGN	✓
UDF3	2.543	9 ± 1	519 ± 38	234 ± 47	4.9 ± 0.3	0.2	4.0 ± 1.6	4^{+4}_{-2}	77	1.8	Galaxy	✓
UDF5	1.759	2.4 ± 0.3	85 ± 6	404 ± 85	0.77 ± 0.04	–	4.6 ± 2.2	$1.3^{+2.0}_{-0.4}$	153	–	–	**nd**
UDF8	1.549	6.5 ± 0.3	100 ± 5	992 ± 50	1.10 ± 0.06	14	2.4 ± 1.3	$1.0^{+1.0}_{-0.5}$	100	36.3	AGN	✓
UDF10	2.086	2.5 ± 0.3	41 ± 5	917 ± 137	0.41 ± 0.05	1	1.9 ± 1.3	$0.6^{+0.4}_{-0.3}$	146	0.6	Galaxy	✗
UDF11	1.9962	6.4 ± 0.9	241 ± 19	380 ± 82	2.2 ± 0.2	0.5	1.46 ± 0.66	$0.6^{+0.7}_{-0.3}$	25	1.7	Galaxy	✗
UDF13	2.497	6.5 ± 1.4	111 ± 17	879 ± 149	1.2 ± 0.2	0.8	1.20 ± 0.68	$0.5^{+0.5}_{-0.2}$	45	2.1	Galaxy	✓
ALESS067.1	2.1212	29 ± 3	487 ± 24	903 ± 100	5.4 ± 0.3	0.4	10 ± 4	8^{+8}_{-4}	164	3.8	Galaxy	✓
AzTEC.GS25	2.292	8 ± 2	401 ± 20	290 ± 88	3.9 ± 0.2	1	13.6 ± 8.2	4^{+4}_{-2}	100	6.1	Galaxy	✓
AzTEC.GS21	1.910	18 ± 2	360 ± 18	746 ± 105	3.9 ± 0.2	0.3	5.8 ± 1.4	5^{+5}_{-2}	139	1.7	Galaxy	✓
AzTEC.GS22	1.794	5.7 ± 0.5	91 ± 5	940 ± 74	1.01 ± 0.06	–	14 ± 8	5^{+5}_{-2}	550	–	–	**nd**
UDF2	2.6961^a	13 ± 3^a	187^{+35a}_{-16}	–	–	–	$7.8^{+1.2b}_{1.0}$	Table 6	Table 6	–	–	**nd**

Notes. The AGN fractions (1) reported above are the ones inferred by using the MIR-X-ray correlation by Asmus et al. (2015); cf. Pantoni et al. (2021, their section 4.4.2). The dust masses (2) listed above include the correction by Magdis et al. (2012) of a factor of ~2. Gas masses (3) are derived from the dust continuum flux at $\lambda = 850$ µm, following Scoville et al. (2016, cf. their fig. 1); see also Pantoni et al. (2021, their section 4.3 and in particular their equation 5). In column **AGN**, we take into consideration any evidence of the presence of an AGN, as reported by Luo et al. (2017): ✓ means that the galaxy has a signature of AGN; ✗ means that the object is classified as a normal star-forming galaxy; **nd** stands for *not detected*. For reference, we list the same available information for UDF2 by [a]Boogaard et al. (2019) and [b]Kaasinen et al. (2020).

Table 6. Spatially resolved properties of the 11 DSFGs in our sample and information derived from CO emission lines. We list (in the order): galaxy ID; spectroscopic redshift (references in Table 1); optical (H_{160}) circularized radius ($r_{\rm H}$); thermal dust circularized radius by ALMA continuum ($r_{\rm ALMA}$); CO circularized radius ($r_{\rm CO}$); optical-to-ALMA size ratio ($r_{\rm H}/r_{\rm ALMA}$); optical-to-CO size ratio ($r_{\rm H}/r_{\rm CO}$); *HST* morphology in the filter H_{160}; CO transition upper level ($J^{\rm up}$); CO line luminosity ($L_{\rm CO}$); H_2 mass (M_{H_2}); and gas depletion time-scale ($\tau_{\rm depl}$).

ID	$z_{\rm spec}$	$r_{\rm H}$ (kpc)	$r_{\rm ALMA}$ (kpc)	$r_{\rm CO}$ (kpc)	$r_{\rm H}/r_{\rm ALMA}$	$r_{\rm H}/r_{\rm CO}$	$r_{\rm CO}/r_{\rm ALMA}$	Morphology H_{160}	$J^{\rm up}$	$L_{\rm CO}$ (10^8 K km s^{-1} pc^2)	M_{H_2} (10^{10} $M_\odot$)	$\tau_{\rm depl}$ (Myr)
UDF1	2.698	2.6	0.46	<3.3	5.7	–	–	Isolated	3	31 ± 3	2.6 ± 0.7	74
UDF3	2.543	1.6	0.62	1.35	2.6	1.2	2.2	Clumpy?	3	170 ± 10	15 ± 3	289
UDF5	1.759	2.3	<2.5	–	–	–	–	Clumpy	–	–	–	–
UDF8	1.549	5.7	4.1	3.45	1.4	1.7	0.9	Isolated	2	122 ± 9	5.8 ± 1.1	580
UDF10	2.086	2.0	<2.5	–	–	–	–	Clumpy	–	–	–	–
UDF11	1.9962	4.5	3.4	–	1.3	–	–	Clumpy	–	–	–	–
UDF13	2.497	1.2	<0.65	–	–	–	–	Isolated	–	–	–	–
ALESS067.1	2.1212	6.5	1.1	3.6	6.0	1.8	3.3	Clumpy	3	196 ± 31	16.8 ± 5.4	345
									6	123 ± 45		
AzTEC.GS25	2.292	1.8	1.2	–	1.5	–	–	Isolated	–	–	–	–
AzTEC.GS21	1.910	3.7	<0.7	–	–	–	–	Clumpy	–	–	–	–
AzTEC.GS22	1.794	3.2	<1.7	–	–	–	–	Clumpy	–	–	–	–
UDF2	2.6961^a	2.5^b	$0.6^{(*)}$	2.6^c	4.3	0.97	4.3	Clumpy^b	3^a	279 ± 33^a	23.9 ± 4.9^a	1300^a

Notes. For reference, we list the same information for UDF2 by [a]Boogaard et al. (2019), [b]Rujopakarn et al. (2019), and [c]Kaasinen et al. (2020). (∗)Rujopakarn et al. (2019) find a core component of 0.3 kpc and a disc component of 1.2 kpc (circularized radii).

support balances the gravitational pull of the inflowing gas (Lapi et al. 2018, their equations 16 and 17). The scenario predicts that the star-forming progenitors of local ETGs experience, at high-z, a dusty burst of star formation in the very central region of the galaxy, at radii $\lesssim R_{\rm rot}$ (red solid line with its 1-σ scatter in Fig. 4), that is traced by the size of dust continuum in the (sub-)millimetre band. At greater radii, i.e. $R_{\rm rot} \lesssim r \lesssim R_{\rm Q}$ (blue solid line with its 1-σ scatter in Fig. 4), the star formation is less obscured by dust, so that UV/optical radiation from newly formed stars can partially emerge. This trend is present in all the six sources of our sample that are resolved both in the *HST* H_{160} (optical sizes; filled squares in Fig. 4) and the ALMA continuum maps (millimetre sizes; filled stars in Fig. 4), i.e. UDF1, UDF3, UDF8, UDF11, ALESS067.1 and AzTEC.GS25, for which the optical size is more extended than the millimetre one. The median optical-to-millimetre radii ratio, i.e. $r_{\rm H}/r_{\rm ALMA} = 2.05$, may be just a lower limit of the real situation, since a significant part of the stellar emission could be lost, being completely absorbed by dust. Furthermore, the ratio $r_\star/r_{\rm dust}$ for our high-z objects behaves differently than for local samples of similar stellar mass (e.g. Lang et al. 2019), being typically larger than 1 for the former and smaller than 1 for the latter.

For reference, in Fig. 4 we show the position of UDF2 (grey filled symbols) that was detected in the ALMA 1.3-mm survey by Dunlop et al. (2017) at $z_{\rm spec} = 2.6961$ (Aravena et al. 2019, Boogaard et al. 2019, González-López et al. 2019, Boogaard et al. 2020; source ID: ASPECS-LP.3mm.07). We stress that the source is not included in our sample since it has no counterpart in the GOODS-MUSIC catalogue by Grazian et al. (2006), within the searching radius of 1 arcsec (more details in Pantoni et al. 2021, cf. their section 2). Its physical properties are very similar to our 11 DSFGs. It has a stellar mass $M_\star = (1.3 \pm 0.3) \times 10^{11}$ $M_\odot$ and it forms stars at a rate of SFR $= 187^{+35}_{-16}$ $M_\odot$ yr^{-1} (see Table 5 and Boogaard et al. 2019,

Table 7. Median, first and third quartiles of the following quantities (in the order): redshift (z); age of the burst ($\tau_\star$); SFR; stellar mass ($M_\star$); IR luminosity ($L_{\rm IR}$); dust mass ($M_{\rm dust}$); molecular gas mass ($M_{\rm gas}$); depletion time ($\tau_{\rm depl}$); AGN fraction in the IR domain ($f_{\rm AGN}$); 2–10 keV luminosity ($L_{\rm X}$); *HST*, ALMA, and CO sizes ($r_{\rm H}$, $r_{\rm ALMA}$, and $r_{\rm CO}$); optical-to-ALMA size ratio ($r_{\rm H}/r_{\rm ALMA}$); optical-to-CO size ratio ($r_{\rm H}/r_{\rm CO}$); and CO-to-ALMA size ratio ($r_{\rm CO}/r_{\rm ALMA}$). For reference, in the last column we list the values measured for UDF2 by Boogaard et al. (2019), Rujopakarn et al. (2019), and Kaasinen et al. (2020), as already referenced in Tabs. 5 and 6.

		Median	1st quartile	3rd quartile	UDF2
z		2.086	1.794	2.497	2.6961
SFR	($\mathrm{M_\odot\ yr^{-1}}$)	241	91	401	187
$\tau_\star$	(Myr)	746	334	917	–
$M_\star$	($10^{10}\ \mathrm{M_\odot}$)	6.5	5.7	9	13
$L_{\rm IR}$	($10^{12}\ \mathrm{L_\odot}$)	2.2	1.01	3.9	–
$M_{\rm dust}$	($10^{8}\ \mathrm{M_\odot}$)	4.6	1.9	10	7.8
$M_{\rm gas}$	($10^{10}\ \mathrm{M_\odot}$)	4.0	0.6	5.8	23.9
$\tau_{\rm depl}$	(Myr)	146	74	345	1300
$f_{\rm AGN}$	(%)	0.8	0.4	1	–
$L_{\rm X}$	(10^{42} erg $\mathrm{s^{-1}}$)	1.7	2.1	6.1	nd
$r_{\rm H}$	(kpc)	2.6	1.8	4.5	2.5
$r_{\rm ALMA}$	(kpc)	1.15	0.6	3.4	0.6
$r_{\rm CO}$	(kpc)	3.45	1.35	3.6	2.6
$r_{\rm H}/r_{\rm ALMA}$		2.05	1.4	5.7	4.3
$r_{\rm H}/r_{\rm CO}$		1.7	1.2	1.8	0.97
$r_{\rm CO}/r_{\rm ALMA}$		2.2	0.9	3.3	4.3

Note. To compute the gas mass value reported above, we preferred the measurements from CO spectral lines (Table 6) rather than the ones from dust continuum (Table 5).

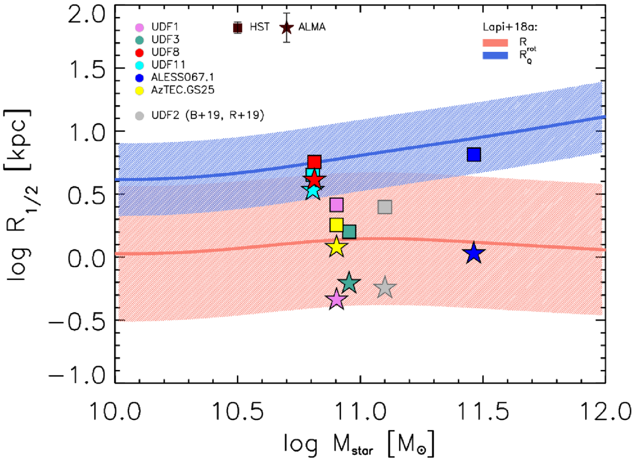

Figure 4. $\mathrm{H_{160}}$ *HST* sizes (filled squares) and ALMA continuum sizes (filled stars) for the six galaxies that are resolved in the continuum ALMA maps: UDF1 (lilac); UDF3 (green); UDF8 (red); UDF11 (cyan); ALESS067.1 (cyan); and AzTEC.GS25 (yellow). Grey filled symbols stand for UDF2 by Boogaard et al. (2019, B + 19) and Rujopakarn et al. (2019, R + 19) that we show as an example of the typical outcomes from similar spatially resolved and panchromatic studies on $z \sim 2$ dusty star-forming galaxies. Blue and red shaded areas represent the predicted behaviour (with its 1σ scatter) of $R_{\rm Q}$ and $R_{\rm rot}$ by the theoretical scenario presented in Lapi et al. (2018). Error bars, consistent with the scatter of the relations, have been omitted for clarity. Typical errors on *HST* and ALMA sizes are shown in the legend.

source ID: ASPECS-LP.3mm.07). Its spatially resolved continuum emission, both in the optical ($\mathrm{H_{160}}$) and in the (sub-)millimetre (ALMA B7), is analyzed in details by Rujopakarn et al. (2019). For the sake of consistency and to compare with our results, we measure the dust size on the same ALMA map (publicly available in the ALMA archive; ALMA project code: 2017.1.00001.S; Member ous: A001/X1288/X4c3) and calculate a circularized ALMA radius of $r_{\rm B7} \approx 0.6$ kpc, while Rujopakarn et al. (2019) measure a core component of $\approx$0.3 kpc and a disc component of $\approx$1.2 kpc (circularized radii; see Table 6). The circularized $\mathrm{H_{160}}$ radius, i.e. $r_{\rm H} \approx 2.5$ kpc (Table 6), is obtained from the effective radius by Rujopakarn et al. (2016), i.e. $r_{\rm e} = 3.71 \pm 0.06$ kpc by assuming the axes ratio by van der Wel et al. (2012). As for the other sources in our sample, also the *HST* and ALMA sizes of UDF2 are in good agreement with the size–mass relation predicted by Lapi et al. (2018) and shown in Fig. 4.

On the one hand, this evidence further confirms that our approach may be applied to other high-z DSFGs with similar multiband coverage of their SED and spectral information in the case spatially resolved images are available in the FIR and UV/optical rest frame. On the other hand, it stresses again the great importance of multiwavelength imaging at great spatial resolution in order to probe galaxy evolution.

More than half of the objects in our sample (i.e. UDF5, UDF10, UDF11, ALESS067.1, AzTEC.GS21, AzTEC.GS22), as well as UDF2 (see Table 6), show a clumpy morphology in the $\mathrm{H_{160}}$ image. This may be suggestive of interactions within a radius $\lesssim$ a few tens of kpc from the ALMA counterpart. However, the optical clumps may just indicate that some emitting areas in the star-forming regions are affected more than others by dust extinction (indeed they are often indicated as *star-forming clumps*). In order to discern the most likely scenario, it is essential to take into consideration galaxy multiwavelength emission and its spatial distribution at comparable resolutions. In Appendix A, we provide an insight on this topic for each galaxy in our sample.

Furthermore, atomic and molecular spectral lines provide essential information to investigate the mechanisms triggering star formation in galaxies and galaxy-BH co-evolution. CO lines are very well recognized as tracers of the cold (i.e. molecular) gas phase and the analysis of their resolved emission, both in space and frequency, allows to study gas kinematics and physical conditions and to measure its content in mass. We identified some differences in the molecular gas masses estimated by using the dust optically thin continuum and CO lines that obviously imply diverse depletion timescales $\tau_\star$ (cf. Tables 5 and 6). These differences can be traced back to diverse dust and CO sizes, the latter being typically larger than the former and its emission almost optically thick (especially in case of low-J CO lines). As such, gas masses inferred from these measurements may sample different regions or components in the galaxy (e.g. Riechers et al. 2011; Hodge et al. 2015; Spilker et al. 2015; Decarli et al. 2016b).

For the four sources in our sample with detected CO lines (i.e. UDF1, UDF3, UDF8, and ALESS067.1), and also for UDF2, the cold gas emission is equally or more extended than the ALMA B7 and B6 continuum (typically $r_{\rm CO}/r_{\rm ALMA} \gtrsim 1$), while it is equal or more compact than the optical emission (see Table 6). This is consistent with the size evolution scenario presented in Lapi et al. (2018) according to which the CO emission traces the rotating cold gas phase that, while inflowing towards the central regions of the galaxy, fuels both the mildly obscured star formation at larger radii (traced by the emission in the optical) and the highly obscured star formation in the innermost regions (sampled by the dust continuum in the (sub-)millimetre).

Furthermore, multiwavelength observations at high spectral and spatial resolution can reveal the presence of nuclear activity. In particular, structure in the CO emission may trace molecular outflows associated with AGN feedback. For example, the X-ray emission properties combined with the double-peak CO line profile of UDF8 are strongly suggestive of the presence of nuclear-driven outflows. This interpretation is also consistent with the age of UDF8 and its SFR (i.e. $\tau_\star \sim 1$ Gyr and SFR $\sim 100\ \mathrm{M}_\odot\ \mathrm{yr}^{-1}$; cf. Table 5) in the galaxy-BH co-evolution scenario by Mancuso et al. (2016b) and Mancuso et al. (2017). A more detailed analysis for UDF8 is given in Appendix A.

6 SUMMARY AND CONCLUSIONS

We have complemented the panchromatic study of the 11 DSFGs, spectroscopically confirmed to be at the peak of cosmic SFH, presented in Pantoni et al. (2021), by focusing on the ALMA view of the galaxies. We selected the 11 objects in the (sub-)millimetre regime requiring the following criteria to be fulfilled for each galaxy: three or more detections in the optical domain; six or more detections in the NIR + MIR bands; two or more detections in the FIR band; spectroscopically confirmed redshift in the range $1.5 < z < 3$; and one or more detections and/or upper limits in the radio and X-ray regimes. The sources are located in one of the deepest multiband field currently available, the GOODS-S. In Pantoni et al. (2021), we exploited the photometry from the X-ray to the radio band to model galaxy SED and extract the main astrophysical properties of the 11 DSFGs (e.g. SFR, stellar mass, stellar attenuation law by dust, dust temperature, IR luminosity, dust and gas mass, AGN fraction).

In this work, we exploited the most recent ALMA continuum maps and spectroscopic images of our 11 DSFGs, selected to have the highest spatial and spectral resolution between the ones publicly available in the ALMA archive. We derived the dust emission size (or just an upper limit in case of scarce spatial resolution) of the 11 DSFGs in our sample; we analyzed the CO $J > 1$ emission lines that we found in the ALMA archive for four of our galaxies (i.e. UDF1, UDF3, UDF8, and ALESS067.1) and derived the molecular hydrogen mass; we compare the outcomes in the (sub-)millimetre regime with galaxy emission in the other spectral bands, such as optical, X-ray, and radio. Finally, we used our findings to put each galaxy in the broader context of galaxy formation and evolution, mainly by referring to the *in situ* galaxy-BH co-evolution scenario (e.g. Mancuso et al. 2016a, b, 2017; Lapi et al. 2018; Pantoni et al. 2019). In the following, we summarize our main results.

(i) We derived the ALMA continuum size of our 11 DSFGs by using the ALMA map at higher spatial resolution currently available in the ALMA archive (ALMA B6, B7, B9). We performed a 2D Gaussian fitting of each source on the *science-ready* image using the task *imfit* embedded in the CASA viewer. More than half of the sources (6 out of 11) are resolved and the median physical size is 1.15 kpc. We interpret this radius as a measure of the region where the bulk of dusty star formation is occurring. It results to be very compact and always <5 kpc.

(ii) We compared the ALMA continuum sizes with the *HST*/WFC3 H_{160} radii (van der Wel et al. 2012). The latter spectral band samples the optical rest-frame emission from stars and traces the star formation of the galaxy that is mildly obscured by dust or unobscured. We found a median ratio between *HST* and ALMA sizes of $r_{\mathrm{H}}/r_{\mathrm{ALMA}} = 2.05$ and it is always >1, in accordance e.g. with the prediction by the *in situ* scenario for the evolution of high-z massive star-forming galaxies (see Lapi et al. 2018) and with other recent works on high-z DSFGs (e.g. Barro et al. 2013, 2016a, b; Ikarashi et al. 2015; Simpson et al. 2015; Massardi et al. 2018; Talia et al. 2018; Tadaki et al. 2020). After correcting for the astrometric shift between H_{160} *HST* maps and ALMA maps, the bulks of the stellar and dust emission coincide within the uncertainties of the astrometric correction (∼100 mas) and the beam resolution for most of the galaxies. An eventual remaining shift tells us that the peaks of optical and (sub-)millimetre emission are not exactly coincident due to dust obscuration of stellar light.

(iii) We analyzed the five CO $J > 1$ emission lines that we found for four of our 11 DSFGs, i.e. UDF1, UDF3, UDF8, and ALESS067.1, and derived the (sub-)millimetre redshift of the sources. The double-peaked spectral line profile of three CO lines, along with their velocity and velocity dispersion maps, is consistent with both a rotating disc of molecular gas and an AGN outflow. In particular, the latter is the case of ALESS067.1, for which we detected two CO lines ($J = 3$ and $J = 6$). The mom1 and mom2 maps suggest the presence of an outflow, even if the associated velocity that is $<500\ \mathrm{km\,s}^{-1}$ does not allow us to confirm this scenario. ALESS067.1 CO (6-5) line is narrow and could trace also the warm star formation in the galaxy (to confirm this interpretation, it is necessary to reconstruct the CO SLED). The narrow single-peaked CO (3-2) line of UDF1 is consistent with a *faced-on* rotating molecular gas disc.

(iv) We derive the molecular gas mass of UDF1, UDF3, UDF8, and ALESS067.1 from the lower J CO emission line luminosity by assuming the CO excitation ladder by Daddi et al. (2015). The median molecular hydrogen gas mass is $\mathrm{M}_{H_2} \sim 1.4 \times 10^{11}\ \mathrm{M}_\odot$. We measured the CO emission size from the distance between the two components peaks (in case of a double-peaked profile) or we give just an upper limit on it, since the sources are not resolved in the mom0 maps. The median CO size is of 3.5 kpc. The CO emission extends over an area greater or equal to the dust continuum size.

(v) We complemented these results by exploiting multiwavelength images from public catalogues that allowed us to include in our final interpretation every signature of galaxy merging/interactions and AGN feedback. The compact FIR and radio sizes ($\lesssim$ a few kpc) of our DSFGs, together with their optical radii (∼2−7 kpc), suggest that the bulk of their star formation can be traced back to *in situ* condensation processes. Almost half of our sources shows an optical isolated morphology, while six galaxies (UDF5, UDF10, UDF11, ALESS067.1, AzTEC.GS21, and AzTEC.GS22) have more complex (i.e. clumpy or disturbed) morphologies but still on scales ∼5−10 kpc. They may indicate the presence of minor interactions – that can prolong the star formation in the dominant galaxy by refuelling it with gas – or may be just a signature of the ongoing dusty star formation.

(vi) We can state that most of the galaxies in our sample are caught in the *gas compaction* phase and models predict that they should be quenched by the AGN feedback in $\sim 10^8$ yr. Three objects show some features that can be interpreted as signatures of nuclear activity by the detection of possible AGN-driven molecular outflows (UDF3, UDF8, and ALESS067.1). After quenching, galaxy evolution should be mainly driven by stellar populations aging and mass additions by dry merger events. Ultimately, we expect our 11 DSFGs to become compact quiescent galaxies or massive ETGs.

(vii) We gathered together all the evidences coming from galaxy multiwavelength emission, gas spectroscopy, and imaging at highest resolution currently available, along with a possible self-consistent and physically motivated theoretical model describing massive star-forming galaxy evolution (e.g. Mancuso et al. 2016a, b, 2017; Lapi et al. 2018; Pantoni et al. 2019). In such a way, we provide a novel approach in characterizing the individual DSFGs and predicting their subsequent evolution.

(viii) Finally, we stress the need of more sensitive multiwavelength maps and higher spatial and spectral resolution images in the diverse spectral bands to definitely clarify the relative impact of *in situ* processes, galaxy interactions, and AGN feedback in determining massive star-forming galaxy evolution at high-z and their morphological transformation.

ACKNOWLEDGEMENTS

The authors thank the anonymous referee for stimulating and constructive suggestions that helped to improve this study. LP gratefully thanks M. Bischetti, S. Campitiello and C. Memo for the useful and helpful discussions, comments, and/or support. LP further thanks I. Smail for his very welcomed comments on the analysis of ALESS067.1 presented here.

This paper makes use of the following ALMA data: ADS/JAO.ALMA#2012.1.00173.S (PI: Dunlop); #2012.1.00307.S (PI: Hodge); #2012.1.00983.S (PI: Leiton); #2015.1.00098.S (PI: Kohno); #2015.1.01074.S (PI: Inami); #2016.1.00564.S (PI: Weiss); #2016.1.01079.S (PI: Bauer); #2017.1.00270.S (PI: Walter); #2017.1.00001.S (PI: Rujopakarn); #2017.1.01347.S (PI: Pope); and #2019.2.00246.S (PI: Calistro Rivera). ALMA is a partnership of ESO (representing its member states), NSF (USA), and NINS (Japan), together with NRC (Canada), NSC and ASIAA (Taiwan), and KASI (Republic of Korea), in cooperation with the Republic of Chile. The Joint ALMA Observatory is operated by ESO, AUI/NRAO, and NAOJ.

We acknowledge financial support from the grants: PRIN MIUR 2017 prot. 20173ML3WW 001 and PRIN MIUR 2017 prot. 20173ML3WW 002 (‘Opening the ALMA window on the cosmic evolution of gas, stars, and massive black holes’). AL is supported by the EU H2020-MSCAITN-2019 project 860744 ‘BiD4BEST: Big Data applications for Black hole Evolution STudies’.

DATA AVAILABILITY

This article uses public data products from ALMA Archive (repository available at the following link: https://almascience.nrao.edu/asax/). Project codes of interest are listed in the Acknowledgements.

H_{160} (F160W) *HST*/WFC3 images are taken from the Hubble Legacy Archive (https://hla.stsci.edu/hlaview.html).

Photometry in the optical, infrared, radio, and X-rays comes from (in the order):

(i) GOODS-MUSIC sample: a multicolour catalogue of near-IR selected galaxies in the GOODS-South field (Grazian et al. 2006), available at the link: https://cdsarc.unistra.fr/viz-bin/cat/J/A + A/449/951 – VizieR DOI: 10.26093/cds/vizier.34490951;

(ii) combined PEP/GOODS-Herschel data of the GOODS fields by Magnelli et al. (2013, https://www.mpe.mpg.de/ir/Research/PEP/DR1) and publicly available at http://www.mpe.mpg.de/ir/Research/PEP/public_data_releases.php (see also https://cdsarc.unistra.fr/viz-bin/cat/J/A + A/528/A35 – VizieR DOI: 10.26093/cds/vizier.35280035);

(iii) Herschel Multi-tiered Extragalactic Survey: HerMES (Oliver et al. 2012), publicly available through the Herschel Database in Marseille, HeDaM, at http://hedam.oamp.fr/HerMES and https://cdsarc.unistra.fr/viz-bin/cat/VIII/95 and https://cdsarc.unistra.fr/viz-bin/cat/VIII/103 (VizieR);

(iv) Very Large Array 1.4-GHz survey of the Extended Chandra Deep Field South: second data release (Miller et al. 2013), https://cdsarc.unistra.fr/viz-bin/cat/J/ApJS/205/13 – VizieR DOI: 10.26093/cds/vizier.22050013;

(v) Very Large Array 6-GHz imaging by Rujopakarn et al. (2016): Project ID VLA/14A-360 (follow-up of the B6 ALMA sources by Dunlop et al. 2017, in the HUDF-S; ADS/JAO.ALMA#2012.1.00173.S); and

(vi) Chandra Deep Field-South survey: 7 Ms source catalogues (Luo et al. 2017), https://cdsarc.unistra.fr/viz-bin/cat/J/ApJS/228/2 (VizieR).

REFERENCES

Aravena M. et al., 2016a, MNRAS, 457, 4406
Aravena M. et al., 2016b, ApJ, 833, 68
Aravena M. et al., 2019, ApJ, 882, 136
Asmus D., Gandhi P., Hönig S. F., Smette A., Duschl W. J., 2015, MNRAS, 454, 766
Bacon R. et al., 2017, A&A, 608, A1
Barro G. et al., 2013, ApJ, 765, 104
Barro G. et al., 2016a, ApJ, 820, 120
Barro G. et al., 2016b, ApJ, 827, L32
Bayet E., Gerin M., Phillips T. G., Contursi A., 2009, MNRAS, 399, 264
Beckwith S. V. W. et al., 2006, AJ, 132, 1729
Béthermin M. et al., 2014, A&A, 567, A103
Bianchini F., Fabbian G., Lapi A., Gonzalez-Nuevo J., Gilli R., Baccigalupi C., 2019, ApJ, 871, 136
Biggs A. D. et al., 2011, MNRAS, 413, 2314
Bischetti M. et al., 2021, A&A, 645, A33
Boogaard L. A. et al., 2019, ApJ, 882, 140
Boogaard L. A. et al., 2020, ApJ, 902, 109
Boquien M., Burgarella D., Roehlly Y., Buat V., Ciesla L., Corre D., Inoue A. K., Salas H., 2019, A&A, 622, A103
Bothwell M. S. et al., 2013, MNRAS, 429, 3047
Bruzual G., Charlot S., 2003, MNRAS, 344, 1000
Calistro Rivera G. et al., 2018, ApJ, 863, 56
Calura F. et al., 2017, MNRAS, 465, 54
Carilli C. L., Walter F., 2013, ARA&A, 51, 105
Carniani S. et al., 2019, MNRAS, 489, 3939
Casey C. M., 2012, MNRAS, 425, 3094
Casey C. M., Narayanan D., Cooray A., 2014, Phys. Rep., 541, 45
Chabrier G., 2003, PASP, 115, 763
Chen C.-C. et al., 2017, ApJ, 846, 108
Cicone C. et al., 2014, A&A, 562, A21
Comastri A. et al., 2011, A&A, 526, L9
Cowie L. L., González-López J., Barger A. J., Bauer F. E., Hsu L. Y., Wang W. H., 2018, ApJ, 865, 106
Cresci G., Maiolino R., 2018, Nature Astron., 2, 179
da Cunha E. et al., 2021, preprint (arXiv:2106.08566)
Daddi E. et al., 2015, A&A, 577, A46
Davé R., Anglés-Alcázar D., Narayanan D., Li Q., Rafieferantsoa M. H., Appleby S., 2019, MNRAS, 486, 2827
Decarli R. et al., 2016a, ApJ, 833, 69
Decarli R. et al., 2016b, ApJ, 833, 70
Di Teodoro E. M., Fraternali F., 2015, MNRAS, 451, 3021
Dickinson M., GOODS Legacy Team, 2001, in American Astronomical Society Meeting Abstracts, Vol. 198. p. 25.01
Donevski D. et al., 2020, A&A, 644, A144
Draine B. T., 2003, ARA&A, 41, 241
Dudzevičiūtė U. et al., 2020, MNRAS, 494, 3828
Dunlop J. S. et al., 2017, MNRAS, 466, 861
Elbaz D. et al., 2018, A&A, 616, A110
Franco M. et al., 2018, A&A, 620, A152
Fujimoto S., Ouchi M., Shibuya T., Nagai H., 2017, ApJ, 850, 83
Gaia Collaboration, 2016, A&A, 595, A2

Giavalisco M. et al., 2004, ApJ, 600, L93
González-López J. et al., 2019, ApJ, 882, 139
Grazian A. et al., 2006, A&A, 449, 951
Hatsukade B. et al., 2018, PASJ, 70, 105
Hodge J. A., Riechers D., Decarli R., Walter F., Carilli C. L., Daddi E., Dannerbauer H., 2015, ApJ, 798, L18
Hodge J. A. et al., 2019, ApJ, 876, 130
Hollenbach D. J., Tielens A. G. G. M., 1999, Rev. Mod. Phys., 71, 173
Huynh M. T. et al., 2017, MNRAS, 467, 1222
Ibar E., Ivison R. J., Biggs A. D., Lal D. V., Best P. N., Green D. A., 2009, MNRAS, 397, 281
Ibar E., Ivison R. J., Best P. N., Coppin K., Pope A., Smail I., Dunlop J. S., 2010, MNRAS, 401, L53
Ikarashi S. et al., 2015, ApJ, 810, 133
Joblin C. et al., 2018, A&A, 615, A129
Kaasinen M. et al., 2020, ApJ, 899, 37
Kellermann K. I., Fomalont E. B., Mainieri V., Padovani P., Rosati P., Shaver P., Tozzi P., Miller N., 2008, ApJS, 179, 71
Kriek M. et al., 2007, ApJ, 669, 776
Kurk J. et al., 2013, A&A, 549, A63
Labbé I. et al., 2015, ApJS, 221, 23
Lacey C. G. et al., 2016, MNRAS, 462, 3854
Lang P. et al., 2019, ApJ, 879, 54
Lapi A. et al., 2018, ApJ, 857, 22
Lo Faro B., Buat V., Roehlly Y., Alvarez-Marquez J., Burgarella D., Silva L., Efstathiou A., 2017, MNRAS, 472, 1372
Luo B. et al., 2017, ApJS, 228, 2
Lutz D. et al., 2011, A&A, 532, A90
Madau P., Dickinson M., 2014, ARA&A, 52, 415
Magdis G. E. et al., 2012, ApJ, 760, 6
Magnelli B. et al., 2013, A&A, 553, A132
Małek K. et al., 2018, A&A, 620, A50
Mancuso C., Lapi A., Shi J., Gonzalez-Nuevo J., Aversa R., Danese L., 2016a, ApJ, 823, 128
Mancuso C., Lapi A., Shi J., Cai Z. Y., Gonzalez-Nuevo J., Béthermin M., Danese L., 2016b, ApJ, 833, 152
Mancuso C. et al., 2017, ApJ, 842, 95
Massardi M. et al., 2018, A&A, 610, A53
Massardi M. et al., 2021, PASP, 133, 085001
Miller N. A. et al., 2013, ApJS, 205, 13
Mingozzi M. et al., 2018, MNRAS, 474, 3640
Momcheva I. G. et al., 2016, ApJS, 225, 27
Oliver S. J. et al., 2012, MNRAS, 424, 1614
Pantoni L., Lapi A., Massardi M., Goswami S., Danese L., 2019, ApJ, 880, 129
Pantoni L. et al., 2021, MNRAS, 504, 928
Planck Collaboration VI, 2020, A&A, 641, A6
Popesso P. et al., 2009, A&A, 494, 443
Popping G., Somerville R. S., Galametz M., 2017, MNRAS, 471, 3152
Pozzi F., Vallini L., Vignali C., Talia M., Gruppioni C., Mingozzi M., Massardi M., Andreani P., 2017, MNRAS, 470, L64
Riechers D. A., Hodge J., Walter F., Carilli C. L., Bertoldi F., 2011, ApJ, 739, L31
Rieke G. H., Alonso-Herrero A., Weiner B. J., Pérez-González P. G., Blaylock M., Donley J. L., Marcillac D., 2009, ApJ, 692, 556
Rujopakarn W. et al., 2016, ApJ, 833, 12
Rujopakarn W. et al., 2019, ApJ, 882, 107
Scott K. S. et al., 2010, MNRAS, 405, 2260
Scoville N. et al., 2016, ApJ, 820, 83
Sharon C. E., Riechers D. A., Hodge J., Carilli C. L., Walter F., Weiß A., Knudsen K. K., Wagg J., 2016, ApJ, 827, 18
Shi J., Lapi A., Mancuso C., Wang H., Danese L., 2017, ApJ, 843, 105
Shin J., Woo J.-H., Chung A., Baek J., Cho K., Kang D., Bae H.-J., 2019, ApJ, 881, 147
Simpson J. M. et al., 2015, ApJ, 807, 128
Smail I., Walter F., 2014, Messenger, 157, 41
Solomon P. M., Downes D., Radford S. J. E., Barrett J. W., 1997, ApJ, 478, 144
Speagle J. S., Steinhardt C. L., Capak P. L., Silverman J. D., 2014, ApJS, 214, 15
Spilker J. S. et al., 2015, ApJ, 811, 124
Szokoly G. P. et al., 2004, ApJS, 155, 271
Tacconi L. J. et al., 2018, ApJ, 853, 179
Tadaki K.-i. et al., 2015, ApJ, 811, L3
Tadaki K.-i. et al., 2020, ApJ, 901, 74
Talia M. et al., 2018, MNRAS, 476, 3956
Targett T. A. et al., 2013, MNRAS, 432, 2012
Thomson A. P. et al., 2014, MNRAS, 442, 577
Toomre A., 1964, ApJ, 139, 1217
Vallini L., Tielens A. G. G. M., Pallottini A., Gallerani S., Gruppioni C., Carniani S., Pozzi F., Talia M., 2019, MNRAS, 490, 4502
van der Wel A. et al., 2012, ApJS, 203, 24
Vanzella E. et al., 2008, A&A, 478, 83
Walter F. et al., 2016, ApJ, 833, 67
Wang S. X. et al., 2013, ApJ, 778, 179
Weiß A. et al., 2009, ApJ, 707, 1201
Wuyts S., van Dokkum P. G., Franx M., Förster Schreiber N. M., Illingworth G. D., Labbé I., Rudnick G., 2009, ApJ, 706, 885
Xue Y. Q. et al., 2011, ApJS, 195, 10
Yang C. et al., 2017, A&A, 608, A144
Yun M. S. et al., 2012, MNRAS, 420, 957

APPENDIX A: INDIVIDUAL SOURCE ANALYSIS

The panchromatic approach already presented in Pantoni et al. (2021) and here enriched by the analysis of multiwavelength spatially resolved emission and CO spectral lines allows us to provide a self-consistent characterization of the 11 DSFGs, which includes their role in the framework of galaxy formation and evolution. In this Appendix, we put together all the observational evidences and give an insight on the possible evolutionary scenario for the individual galaxies that are in our sample.

While characterizing galaxy cold gas phase, we preferentially use the gas mass measurements from CO spectral lines (when available; see Table 6) rather than the ones from dust continuum (Table 5), since the latter can miss the gas distributed over scales larger than the dust continuum size (e.g. Riechers et al. 2011; Hodge et al. 2015; Spilker et al. 2015; Decarli et al. 2016b).

Finally, we note to the reader that all the multiwavelength radii and sizes presented here are circularized (see equation 2).

A1 UDF1 (J033244.01-274635.2)

UDF1 is a DSFG at $z_{\rm spec} = 2.698$ (see Table 1). We measured its spectroscopic redshift from a CO (3-2) line (Table 4) that is consistent, within the errors, with the redshift of the C[II] emission line at 8600 Å (2330 Å rest frame) by Szokoly et al. (2004; H II region-type spectrum). UDF1 was detected in the ALMA B6 ($\lambda \sim 1.3$ mm) survey by Dunlop et al. (2017) and more recently by Franco et al. (2018) at $\lambda \sim 1.1$ mm (source ID: AGS6). Rujopakarn et al. (2016) detected its radio counterpart with the VLA at 6 GHz. The corresponding fluxes are $S_{1.3\,\rm mm} = 924 \pm 76$ μJy, $S_{1.1\,\rm mm} = 1.26 \pm 0.16$ mJy, and $S_{6\,\rm GHz} = 9.02 \pm 0.57$ μJy. In the ALMA archival continuum map at the best spatial resolution currently available for UDF1 (project code: 2017.1.00001.S, ALMA B7; see Table 2), the source is detected at a significance level of $>5\sigma$. We measure a flux $S_{1\,\rm mm} = 2900 \pm 300$ μJy (Table 2). This flux is consistent with the 850-μm ALMA B7 flux measured by Cowie et al. (2018), i.e. $S_{850\,\mu\rm m} = 3.38 \pm 0.32$ mJy (source ID: no. 22; name ALMA033244-274635) and by Rujopakarn et al. (2019) on the same ALMA map, i.e. $S_{\rm B7} = 3407 \pm 226$ μJy. In the B7 ALMA map the source is resolved: we measure a circularized radius

$r_{\rm ALMA} \simeq 0.46$ kpc, where we expect the dusty star formation to be located. Rujopakarn et al. (2016) find the 6-GHz radio flux to be compatible with the star formation activity of the ALMA source, confirming the outcome we obtained from the analysis of galaxy SED in Pantoni et al. (2021). The radio emission, which samples also the mildly obscured and unobscured star formation of the galaxy, extends over a larger region: $r_{\rm VLA} \sim 2.7$ kpc (FWHM; Rujopakarn et al. 2016). From the CO (3-2) line luminosity we estimate the molecular hydrogen content of the galaxy to be $M_{H_2} = (2.6 \pm 0.7) \times 10^{10}$ M$_\odot$. From its velocity and velocity dispersion maps we claim that the galaxy cold gas component is probably a *faced-on* rotating disc that extends over a radius of $\lesssim 3$ kpc (see Table 3). Its spatial distribution samples the galaxy star formation, both obscured and unobscured, as well as the aforementioned radio emission, which extends over a region of a similar size.

The peak of dust radiation matches pretty well that of stellar emission (the *HST*/WFC3 emission map in the filter H$_{160}$, overlapped by ALMA contours, is shown in Fig. 1). The optical size ($r_{\rm H} \sim 2.6$ kpc; Rujopakarn et al. 2019, see Table 1) extends over a radius that is more than a factor of 5 larger than the ALMA size, reported above and in Table 2. These evidences can be easily ascribed to a very rapid condensation and compaction of the gas towards the centre of the galaxy (over a typical time-scale of $\tau \sim 10^6$ yr), where the bulk of dusty star formation takes place ($M_{\rm dust} \sim 6 \times 10^8$ M$_\odot$, see Tables 1 and 5).

From the analysis presented in Pantoni et al. (2021), UDF1 is almost approaching the galaxy main sequence (see e.g. Speagle et al. 2014) at the corresponding redshift (it is a factor of ∼2× above) with a stellar mass $M_\star = (8 \pm 1) \times 10^{10}$ M$_\odot$ and SFR $= 352 \pm 18$ M$_\odot$ yr^{-1}. We think that it is probably experiencing the last phase of dusty star formation before the intervention of the AGN feedback. Indeed, even if the optical counterpart has been historically classified as a normal star-forming galaxy (the presence of an AGN cannot be established from the optical data alone), it has a very powerful counterpart in the X-ray, suggesting the presence of an accreting central SMBH. In the ≃7 Ms CDFS catalogue by Luo et al. (2017), the X-ray source (IDX 850) is classified as AGN (see Tables 1 and 5). The intrinsic absorption column density[2] $N_{\rm H} \sim 1.2 \times 10^{22}$ cm^{-2} gives an absorption-corrected intrinsic 2−10 keV luminosity of $\sim 4 \times 10^{43}$ erg s^{-1} (see Table 5). Rujopakarn et al. (2016) suggest that the VLA size of UDF1 can be somehow more extended than the ALMA one due to the central AGN, even if the 6-GHz radio flux does not appear to be enhanced, when compared to the one expected from star formation alone. Relying on the prescriptions of the *in situ* scenario for galaxy evolution (see Mancuso et al. 2017), we expect the nucleus radio emission to emerge from the one associated to star formation only at later times.

Gas and dust rich, with a typical depletion time-scale $\tau_{\rm depl} \sim 75$ Myr, we think that UDF1 very compact and intense star formation must have triggered a rapid growth of the central SMBH, whose power in the X-ray clearly overwhelms the host galaxy one (Pantoni et al. 2021). We expect this galaxy to overlap the galaxy main sequence in a few hundreds of Myr and then to be quenched by the central AGN.

A2 UDF3 (J033238.53-274634.6)

UDF3 is a DSFG at $z_{\rm spec} = 2.544^{+0.001}_{-0.002}$ (Table 1) that we measured from a CO (3-2) line detected in an ALMA B3 ($\nu_{\rm obs} \simeq 97.6$ GHz; see Tables 3). Our measurement is consistent, within the errors, with the one by Decarli et al. (2016b), based on the blind detection of three CO transitions (ASPECS 3 mm.1, 1 mm.1, 1 mm.2; Decarli et al. 2016a), i.e. $z_{\rm spec} = 2.543$ (see also Tacconi et al. 2018). Another measurement, consistent with ours, comes from the MUSE HUDF project, i.e. $z_{\rm spec} = 2.541$ (Bacon et al. 2017). Finally, Momcheva et al. (2016) report a grism redshift $z_{\rm spec} \sim 2.561$, based on the detection of the [O II] line in the 3D-*HST* data, that is in accordance with the aforementioned spectroscopic determinations of the source redshift to the second decimal digit.

UDF3 was detected both in the B6 (∼1.3 mm) ALMA continuum and 6-GHz VLA maps of the HUDF by Dunlop et al. (2017) and Rujopakarn et al. (2016). The corresponding fluxes are $S_{1.3\,\rm mm} = 863 \pm 84$ µJy and $S_{6\,\rm GHz} = 12.06 \pm 0.55$ µJy. We found a >5-σ continuum detection for this source in the ALMA B7 (project code: 2017.1.00001.S, Table 2) and we measured a flux $S_{1\,\rm mm} = 1600 \pm 200$ µJy. This flux is in accordance with the 850 -µm ALMA flux measured by Cowie et al. (2018), i.e. $S_{850\,\mu\rm m} = 2000 \pm 400$ µJy (source ID: no. 48; name ALMA033238-274634), and the 1.1-mm ALMA flux measured by Franco et al. (2018), i.e. $S_{1.1\,\mu\rm m} = 1130 \pm 105$ µJy (source ID: AGS12). Rujopakarn et al. (2016) found the 6-GHz radio flux of UDF 3 to be solely compatible with the star formation activity of the galaxy, in agreement with the outcome from our SED analysis (Pantoni et al. 2021). However, they claim that the possible presence of a central AGN could have an impact on the radio size, i.e. $r_{\rm VLA} = 1.5 \pm 0.1$ kpc (FWHM; Rujopakarn et al. 2016). The ALMA (and VLA) source has an X-ray counterpart (IDX 718) in the ≃7 Ms CDFS survey catalogue by Luo et al. (2017). The source 2−10 keV luminosity is 1.8×10^{42} erg s^{-1}. All these evidences suggest that the central BH could be accreting material in the host galaxy nucleus, even if its emission does not clearly overwhelm the X-ray light coming from star formation at the moment (Pantoni et al. 2021).

The rest-frame UV/optical morphology is unclear and may be clumpy/disturbed (see Fig. 1 and Table 6). However, we do not find any clear evidence of interactions. The starlight emission is compact ($r_{\rm H} \sim 1.6$ kpc; van der Wel et al. 2012, see Table 1) and its peak appears to be shifted when compared to the ALMA B7 continuum emission, possibly due to dust obscuration of stellar light. (Fig. 1). The absence of interactions is confirmed by the velocity and dispersion velocity maps of CO (3-2) molecular line that are smooth (i.e. not disturbed) and consistent with a rotating disc of molecular gas (confirmed by the double-peaked profile of the spectral line; see Fig. 2) extending over a radius of ∼1.4 kpc. The (sub-)millimetre source is resolved in the ALMA B7 continuum map: we measure a circularized radius of $r_{\rm ALMA} \sim 0.6$ kpc (Table 2). However, to confirm this scenario we need multiwavelength images at higher spatial resolution.

In the analysis presented in Pantoni et al. (2021), we found UDF3 to be a very young object (age ∼200−300 Myr), forming stars at a rate SFR ∼500 M$_\odot$ yr^{-1} (sSFR ∼5.8 Gyr^{-1}). Fuelled by the large amount of gas and dust ($M_{H_2} = (1.5 \pm 0.3) \times 10^{11}$ M$_\odot$ and $M_{\rm dust} \sim 4 \times 10^8$ M$_\odot$; Tables 1 and 4), its intense burst of star formation (depletion time-scale $\tau_{\rm depl} \lesssim 100$ Myr) must trigger the growth of the central BH that we expect to become active and quench star formation in a few 10^8 yr. In the SFR−$M_\star$ plot, UDF3 lies to the top left side of the main sequence at the corresponding redshift (even if it is still consistent with the 2-σ scatter of the relation; see Speagle

---

[2] The column density N_H (reported here, but also for other sources in our sample, in the following Sections) is derived on the basis of flux ratios in the hard and soft X-ray bands, by assuming a classical AGN slope of 1.8.

et al. 2014; Pantoni et al. 2021). A similar result was found by Elbaz et al. (2018), who classify UDF3 as a starburst galaxy.

A3 UDF5 (J033236.94-274726.8)

UDF5 is a DSFG detected both in the B6 ($\sim$1.3 mm) ALMA and 6-GHz VLA maps of the HUDF by Dunlop et al. (2017) and Rujopakarn et al. (2016). The corresponding fluxes are $S_{1.3\,\mathrm{mm}} = 311 \pm 49$ µJy and $S_{6\,\mathrm{GHz}} = 6.26 \pm 0.46$ µJy.

As to the source redshift, Momcheva et al. (2016) report a $z_{\mathrm{spec}} = 1.759$, basing on 3D-*HST* spectroscopy (Table 1).

For this millimetre source, we do not find any X-ray counterpart in the literature, neither by the association with the $\simeq$7 Ms X-ray catalogue by Luo et al. (2017) nor in the supplementary catalogue at very low significance. This may indicate that either no (i.e. not very powerful) AGN is present or it is highly obscured (i.e. Compton-thick, with $N_{\mathrm{H}} \gtrsim 10^{24}$ cm^{-2}). Since the source lies in a very deep region of the *Chandra* map (equivalent exposure time of about 6.22 Ms), we think that the most probable hypothesis to explain the non-detection is the latter. Following the *in situ* scenario predictions, the central BH must have just started to accrete material from the surroundings; as such, we do not expect to observe any signature of its activity on the source morphology. Both ALMA and VLA sizes can provide a good measure of the region where the bulk of star formation is occurring, i.e. very compact, $\sim$2 kpc ($r_{\mathrm{ALMA}} <$ 2.5 kpc; rVLA $\sim$ 1.5 kpc; see Table 2 and Rujopakarn et al. 2016). Rujopakarn et al. (2016) claim that the 6-GHz VLA flux is solely compatible with the star formation activity of the galaxy, confirming the result by Pantoni et al. (2021).

The *HST*/WFC3 H$_{160}$ circularized radius of UDF5 is $r_{\mathrm{H}} \sim 2.3$ kpc, slightly larger than the radio one and consistent with the upper limit on the ALMA B6 size. The rest-frame optical morphology is clumpy/disturbed (Fig. 1 and Table 6). Since no clear evidence of interactions and/or AGN feedback has been observed, we ascribe the galaxy multiband morphology to both the dust enshrouded star formation occurring at radii $\lesssim$2 kpc and the gas compaction towards the central region.

From the analysis by Pantoni et al. (2021), UDF5 is in the vicinity of the main sequence at the corresponding redshift. This young galaxy (age $\sim$400 Myr) shows a more moderate SFR ($\sim$80$-$90 M$_{\odot}$ yr^{-1}) and a more modest stellar mass (a few 10^{10} M$_{\odot}$) compared to the other galaxies in our sample (cf. Table 1). The depletion timescale is $\tau_{\mathrm{depl}} \lesssim 900$ Myr and the dust content is quite high ($M_{\mathrm{dust}} \sim 4 \times 10^{10}$ M$_{\odot}$). Following the *in situ* scenario, we expect the star formation to last longer than what is seen for the bulk of high-z DSFGs ($\tau_{\mathrm{burst}} \sim$ a few 10^{9} yr). This picture can explain why we do not have any evidence of an active nucleus: less intense burst of star formation implies a slower BH accretion history and at the current galaxy age (i.e. $\sim$400 Myr), the central BH is highly obscured in the X-ray and the emission is still dominated by star formation.

A4 UDF8 (J033239.74-274611.4)

UDF8 is a DSFG at z$_{\mathrm{spec}} \sim 1.6$. The slit redshift $z_{\mathrm{spec}} = 1.552$ by Kurk et al. (2013) matches the CO line detection by Decarli et al. (2016b, source ID: ASPECS3mm.2) and our measurement from the CO (2-1) spectral line detected in the ALMA B3 data cube, i.e. $z_{\mathrm{spec}} = 1.5510^{+0.0014}_{-0.0005}$ (Table 1) that we use in our analysis.

UDF8 was detected both in the B6 ($\sim$1.3 mm) ALMA and 6-GHz VLA maps of the HUDF by Dunlop et al. (2017) and Rujopakarn et al. (2016). The corresponding fluxes are $S_{\mathrm{B6}} = 208 \pm 46$ µJy and $S_{6\,\mathrm{GHz}} = 7.21 \pm 0.47$ µJy. The source is resolved both in ALMA and VLA maps and the corresponding radii are $r_{\mathrm{ALMA}} \sim 4.1$ kpc (Table 2) and $r_{\mathrm{VLA}} \sim 2.1$ kpc. This dusty galaxy, still compact, is, however, more extended in the millimetre than the bulk of high-z DSFGs (typical ALMA radius is found to be $\lesssim$1$-$2 kpc).

In the rest-frame UV/optical the galaxy appears to be isolated (see Fig. 1 and Table 6), suggesting that the bulk of star formation can be traced back to local, *in situ* condensation processes. The galaxy is more extended in the optical ($r_{\mathrm{H}} \sim 5.7$ kpc) than in the millimetre continuum, consistently with what we expect in the gas compaction evolutionary phase. This is confirmed by the double-peaked spectral profile of its CO (2-1) line and the velocity and velocity dispersion maps (Fig. 2), which suggest that we are observing a rotating disc of molecular gas extending over an area of radius $r_{,\mathrm{CO}} \sim 3.5$ kpc. From the CO line luminosity we derive a molecular hydrogen mass $M_{H_2} = (5.8 \pm 1.1) \times 10^{10}$ M$_{\odot}$ that is consistent within the uncertainties with the one estimated by Decarli et al. (2016b), i.e. $M_{H_2} \sim 6.5 \times 10^{10}$ M$_{\odot}$, under the assumption of the same $\alpha_{\mathrm{CO}} = 3.6$ K km pc^2 s^{-1} M$_{\odot}^{-1}$.

UDF8 is detected with *Chandra*. We found its X-ray counterpart (IDX 748) in the $\simeq$7 Ms CDFS survey catalogue by Luo et al. (2017). The source 2$-$10 keV luminosity is 3.5×10^{43} erg s^{-1}, suggesting that UDF8 hosts an active galactic nucleus (see Table 1), which dominates over the X-ray emission of the host galaxy (Pantoni et al. 2021). Even if the galaxy hosts an X-ray AGN, Rujopakarn et al. (2016) claim that its contribution to the radio emission is negligible. Indeed, they find the radio flux at 6 GHz to be consistent with the star formation alone, as to the radio morphology. From the analysis of galaxy SED by Pantoni et al. (2021), we obtain the same outcome.

UDF8 is a main-sequence galaxy of age $\sim$1 Gyr, forming stars at a rate SFR of $\sim$100 M$_{\odot}$ yr^{-1}, with an sSFR $\sim$1.5 Gyr^{-1} (Pantoni et al. 2021). We expect the AGN quenching to be very close: eventually, its effect could be already seen under the shape of outflows and winds that can affect the multiband sizes of UDF8 and broaden its CO (2-1) spectral line profile (with respect to pure disc rotation). To confirm this scenario, we need multiband images at higher spatial resolution of the galaxy nuclear region.

A5 UDF10 (J033240.73-274749.4)

UDF10 is a DSFG at $z_{\mathrm{spec}} = 2.086$ (grism redshift by Momcheva et al. 2016, based on the detection of an optical rest-frame line in the 3D-*HST* data; Table 1).

The galaxy was detected at 3.6σ in the ALMA B6 ($S_{\mathrm{B6}} = 184 \pm 46$ µm) in the blind survey of the HUDF by Dunlop et al. (2017). In the radio (6-GHz VLA Rujopakarn et al. 2016) it is detected at a significance level of $<3\sigma$; thus, only an upper limit of the 6-GHz radio flux of the source is available, i.e. $S_{6\,\mathrm{GHz}} \lesssim 0.70$ µJy. The source is not resolved in the ALMA map, but its size must be <2.5 kpc (Table 2). After the astrometric corrections, the ALMA centroid emission appears to be shifted of $\sim$10 mas from the optical peak (Fig. 1; see also Dunlop et al. 2017). UDF10 optical radius is $r_{\mathrm{H}} \sim 2.0$ kpc (Table 1), that is comparable with the upper limit on ALMA size.

UDF10 is detected with *Chandra* (IDX 756) in the $\simeq$7 Ms CDFS catalogue by Luo et al. (2017). The source 2$-$10 keV luminosity is then 6×10^{41} erg s^{-1}. Luo et al. (2017) classified the source to be a normal galaxy (Table 1).

Putting together these evidences with the outcomes from the galaxy SED analysis presented in Pantoni et al. (2021), UDF10 is a $z \sim 2$ main-sequence galaxy, since it overlaps the corresponding relation by Speagle et al. (2014). Quite old (age $\sim$1 Gyr) when compared to the other sources of the sample, it is characterized by a less intense burst of star formation, with SFR $\sim$40 M$_{\odot}$ yr^{-1} and sSFR is $\sim$1$-$2 Gyr^{-1}. With a slightly smaller dust content ($M_{\rm dust} \sim 2 \times 10^8$ M$_\odot$) than the majority of DSFGs, possibly its star formation has not triggered yet the activity of the central nucleus, whose power is still too low to have any kind of impact on the host galaxy. Indeed, the emission coming from star formation dominates both the radio and the X-rays (Rujopakarn et al. 2016; Pantoni et al. 2021). However, multiwavelength images at higher spatial resolution and sensitivity are crucial to confirm (or reject) this scenario.

A6 UDF11 (J033240.06-274755.5)

UDF11 is a DSFG at $z_{\rm spec} \sim 2$. The most recent redshift measurement comes from the MUSE HUDF project, i.e. $z_{\rm spec} = 1.9962 \pm 0.0014$ (Bacon et al. 2017; Dunlop et al. 2017), in total agreement with the previous deep spectroscopy by Kurk et al. (2013), who exploited the red-sensitive optical spectrograph FORS2 installed at the Very Large Telescope.

UDF11 was detected both in the B6 ($\sim$1.3 mm) ALMA and 6-GHz VLA maps of the HUDF by Dunlop et al. (2017) and Rujopakarn et al. (2016). The corresponding fluxes are $S_{1.3\,\rm mm} = 186 \pm 46$ μJy and $S_{6\,\rm GHz} = 9.34 \pm 0.74$ μJy.

The galaxy is resolved both in ALMA and VLA maps. In the millimetre, it results to be more extended ($r_{\rm ALMA} \sim 3.4$ kpc; see Table 2) than the bulk of high-z DSFGs (typical ALMA radius is found to be $\lesssim$1$-$2 kpc). The radio morphology is well reproduced by a two-components fit: one is spatially coincident with the central ALMA emission ($r_{\rm VLA} \sim 3.4$ kpc) and the other, more compact ($r_{\rm VLA} \sim 0.7$ kpc) but shifted to the sides of the central millimetre emission, could indicate the presence of two radio lobes/hotspots, suggesting the presence of a central radio AGN (Rujopakarn et al. 2016). The radio flux at 6 GHz is solely consistent with the ongoing star formation in the host galaxy, as it is confirmed by the SED analysis presented in Pantoni et al. (2021). Basing on these results, we can assert that the central nucleus is experiencing the radio-quiet (RQ) phase, producing jets that are still not dominant in the radio band. This is partially confirmed by the properties of the X-ray source counterpart (IDX 751) in the *Chandra* 7 Ms catalogue by Luo et al. (2017). The intrinsic absorption column density $N_{\rm H} \sim 3.79 \times 10^{21}$ cm^{-2} gives an absorption-corrected intrinsic 2$-$10 keV luminosity of 1.7×10^{42} erg s^{-1}. Luo et al. (2017) do not find any clear evidence to classify the source as AGN (see Table 1). However, an X-ray luminosity of $>10^{42}$ erg s^{-1} could indicate that a (small) fraction of the emission may be traced back to the central engine. We expect the galaxy to host an RQ AGN, still accreting material.

Also, the *HST*/WFC3 H$_{160}$ radius is more extended ($r_{\rm H} \sim 4.5$ kpc; see Table 1) than the aforementioned ALMA and VLA sizes. The rest-frame optical morphology is clearly clumpy/disturbed (Fig. 1). This evidence could be traced back to some interactions with the ambient, replenishing with gas the galaxy at large radii and fuelling the star formation (that is still ongoing, even if a signature of AGN feedback is observed in the radio band). Alternatively, the optical clumpy morphology could be simply ascribed to the combination of quenching and host galaxy star formation. Note that AGN-driven winds and outflows can locally have a positive impact on star formation, compressing the gas phase and increasing its density at large radii, i.e. $r \gtrsim 1$ kpc (e.g. Cresci & Maiolino 2018; Shin et al. 2019). This may have affected the SED-derived age of the galaxy (which appears younger) and could justify the still high SFR. Multiwavelength imaging at higher resolution is crucial to shed light on this respect.

From the SED analysis by Pantoni et al. (2021), the ongoing star formation burst in UDF11 has an age of $\sim$400 Myr and it is forming stars at a rate SFR of $\sim$250 M$_\odot$ yr^{-1}, with an sSFR of $\sim$4 Gyr^{-1}. Showing a more modest gas and dust content (i.e. $M_{\rm gas} \sim 6 \times 10^9$ M$_\odot$ and $M_{\rm dust} \sim (1.5 \times 10^8$ M$_\odot$) than the majority of our DSFGs, UDF11 is characterized by a depletion time-scale of $\tau_{\rm depl} \sim 25$ Myr. We expect the AGN quenching to be close, as it is also confirmed by the extended radio size of the galaxy and the disturbed morphology in the optical, which may be affected by the energetic of the central nucleus. Indeed, in the SFR$-$M$_\star$ plot, UDF11 is indeed almost on the main sequence at the corresponding redshift.

A7 UDF13 (J033235.07-274647.6)

UDF13 is a DSFG at redshift $z_{\rm spec} = 2.497 \pm 0.008$ (grism redshift by Momcheva et al. 2016, based on the 3D-*HST* spectroscopy; see Table 1).

UDF13 was detected both in the B6 ($\sim$1.3 mm) ALMA and 6-GHz VLA maps of the HUDF by Dunlop et al. (2017) and Rujopakarn et al. (2016). The corresponding fluxes are $S_{1.3\,\rm mm} = 174 \pm 45$ μJy and $S_{6\,\rm GHz} = 4.67 \pm 0.53$ μJy. We measure an ALMA B7 continuum flux of $S_{\rm B7} = 910 \pm 170$ μJy and give an upper limit on the ALMA size, i.e. <0.65 kpc (Table 2). We note that the optical radius ($r_{\rm H} \sim 1.2$ kpc; Table 1) is more extended than the upper limit on the millimetre size. In the UV/optical rest frame (Fig. 1), UDF13 appears as an isolated object with a smooth (i.e. undisturbed) morphology.

UDF13 has an X-ray counterpart (IDX 655) in the 7 Ms *Chandra* catalogue by Luo et al. (2017) with a 2$-$10 keV luminosity of 1.3×10^{42} erg s^{-1}. Luo et al. classify it as AGN (Table 1). From the mutual analysis of FIR and radio fluxes of the source, Rujopakarn et al. (2016) found the radio emission to be enhanced by the central AGN detected in the X-ray. This conclusion is derived comparing the observed $S_{5\,\rm cm}/S_{1.3\,\rm mm}$ flux ratio with the one predicted by the Rieke et al. (2009) IR SED libraries that are calibrated on local ULIRGs. This calibration on local Universe dusty galaxies along with the SED libraries intrinsic uncertainties might alter significantly the analysis. From the SED fitting and radio analysis presented in Pantoni et al. (2021), the VLA flux is instead consistent with the ongoing star formation in the host galaxy.

The analysis presented in Pantoni et al. (2021) classifies UDF13 a main-sequence galaxy, confirming the outcome by Elbaz et al. (2018). Quite old (age $\sim$900 Myr) when compared to the other sources of the sample, UDF13 forms stars at a rate SFR of $\sim$100 M$_\odot$ yr^{-1}, with an sSFR of $\sim$1.7 Gyr^{-1}. Showing a more modest gas and dust content ($M_{\rm gas} \sim 5 \times 10^9$ M$_\odot$ and $M_{\rm dust} \sim 1.2 \times 10^8$ M$_\odot$) than the majority of our DSFGs, UDF13 is characterized by a depletion time-scale of $\tau_{\rm depl} \sim 45$ Myr. We expect this galaxy to be soon quenched by the central AGN and to subsequently become a red and dead galaxy.

A8 ALESS067.1 (J033243.19-275514.3)

ALESS067.1 is a DSFG at redshift $z_{\rm spec} = 2.1212^{+0.0014}_{-0.0005}$ (this work from CO (3-2) spectral line, see Table 1). It is consistent with the one measured from an H$_\alpha$ line with the Gemini Near-Infrared Spectrograph by Kriek et al. (2007), i.e. $z_{\rm spec} = 2.122$.

The galaxy (sub-)millimetre counterpart was first observed by LABOCA (LESS; Weiß et al. 2009) and then by ALMA as a part of the ALESS project (Smail & Walter 2014). It is a compact millimetre source, characterized by a radius of $r_{\rm ALMA} \sim 1.1$ kpc (Table 1; but see also Thomson et al. 2014; Fujimoto et al. 2017). We found two continuum detection in ALMA B3 and B4 (project code:

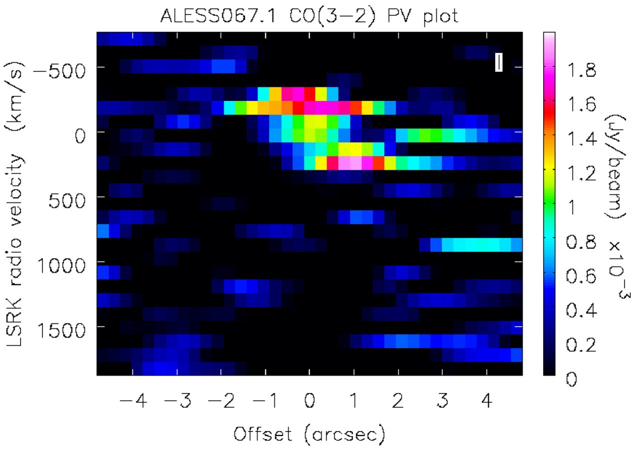

Figure A1. Position velocity diagram for ALESS067.1 CO (3-2) molecular emission line.

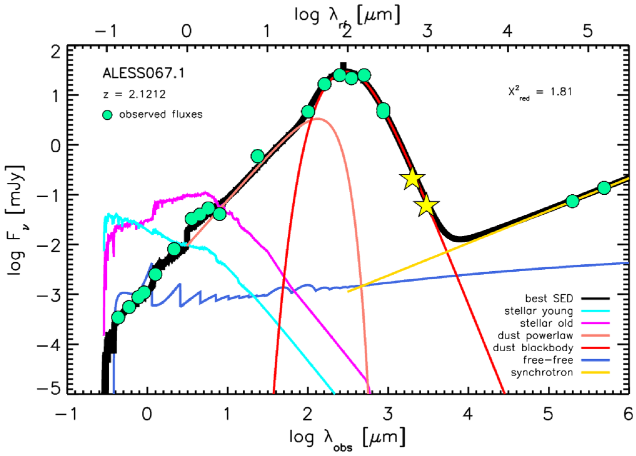

Figure A2. UV-radio best SED for ALESS067.1. Yellow filled stars stand for the ALMA B4 and B3 fluxes measured in this work (see B3 continuum contours in Fig. 3) and are not included in the SED fitting. Green filled circles represent the multiband available photometry. Error bars are omitted when comparable to symbol size.

2016.1.00564.S and 2015.1.00948.S) and we measure the fluxes $S_{B3} = 60 \pm 20$ μJy and $S_{B4} = 190 \pm 70$ μJy.

In the *HST*/WFC3 H_{160} image (Fig. 1), the galaxy shows an extended (i.e. $r_H \sim 6.5$ kpc; Table 1) and disturbed/clumpy morphology (van der Wel et al. 2012; Targett et al. 2013), which could be interpreted either as a signature of an ongoing heavily obscured and intense star formation episode or as a possible indication of some companions (Targett et al. 2013, claim it is the dominant galaxy of a multiple system). We can gain some indications on the overall picture by analyzing the two CO $J > 0$ emission lines detected for ALESS067.1 (see Table 3 and Fig. 3). The velocity map (mom1) of the CO (3-2) line shows a clear velocity gradient that could indicate the presence of a rotating disc of molecular gas. However, the velocity dispersion map (mom2) shows an evident central peak with a high-velocity tail towards the upper left corner, which could indicate the presence of an outflow, possibly due to a central AGN. Similarly, the double-peaked line profile (Fig. 3) could be ascribed either to the inclination of the rotation plane with respect to the line of sight or to the presence of a double outflow powered by the active nucleus, where one jet is receding and the other is approaching the observer. Other hints can be gained by the analysis of the position velocity (pv) diagram (Fig. A1); reference axis goes through the centre and follows the velocity gradient in the velocity map with an inclination of ∼70 degrees). The asymmetric and disturbed appearance of the pv plot may confirm the presence of a double AGN-driven molecular outflow, with a $|v| \simeq 400$ km s^{-1} and a peak of $v \simeq 900$ km s^{-1} (light cyan structure, which actually, might be just noise). A clear interpretation requires higher spectral and spatial resolution in the ALMA cube, which would have allowed to model the CO (3-2) kinematics, exploiting, e.g. 3D-Barolo (Di Teodoro & Fraternali 2015), a tool for fitting 3D tilted-ring models to emission-line data cubes that takes into account the effect of beam smearing. However, we note that the presence of a molecular outflow triggered by a central engine is consistent also with the CO (6-5) velocity map (mom1; Fig. 3), which shows a peak at higher velocities (i.e. ∼100 km s^{-1}) in the orthogonal direction with respect the CO (3-2) peak in the mom1 map. I further note that another possible interpretation is the one suggested by Calistro Rivera et al. (2018) who gave preference to the scenario in which the CO(3-2) line is originated in two sources (one of them is ALESS067.1) possibly in an early stage of merger event (see also Chen et al. 2017).

ALESS067.1 was detected in the X-ray by Luo et al. (2017). Its intrinsic 2-10 keV luminosity is $L_{2-10\,\mathrm{keV}} \simeq 3.8 \times 10^{42}$ erg s^{-1}, once corrected for obscuration (see also Pantoni et al. 2021). In Pantoni et al. (2021) we have already noted that the X-ray luminosity is almost dominated by the host galaxy star formation (see also Wang et al. 2013), however it does not exclude the possible presence of a central accreting nucleus at early stage (cf. Mancuso et al. 2016b, Mancuso et al. 2017), whose activity could have an impact on the unclear galaxy morphology, even if at this point the nucleus emission does not emerge significantly neither in the radio nor in the IR domain (Thomson et al. 2014).

In Fig. A2, we show the full SED of ALESS067.1, already studied in Pantoni et al. (2021). Here, we complete the modelling by including the two galaxy radio fluxes available for the source (cf. their table 2, Pantoni et al. 2021) in the SED fitting. CIGALE modules in the radio band include synchrotron and free–free emission. The resulting stellar mass $M_\star = (2.9 \pm 0.3) \times 10^{11}$ M$_\odot$ and SFR = 485 ± 24 M$_\odot$ yr^{-1} place the source on the main sequence of star-forming galaxies at the corresponding redshift (e.g. Speagle et al. 2014). An almost constant SFH (e.g. Mancuso et al. 2016b) leads to a burst age of ≃0.9 Gyr. The quite huge dust content ($M_{\rm dust} = (5 \pm 2) \times 10^8$ M$_\odot$) is consistent both with predictions from theory (e.g. Popping et al. 2017; Pantoni et al. 2019) and measurements on statistical sample of DSFGs (e.g. Magdis et al. 2012). We find a radio spectral index $\alpha = 0.7 \pm 0.1$ and an FIR/radio flux ratio $q_{\rm IR} = 2.5 \pm 0.1$, in total agreement with the findings by Ibar et al. (2009, 2010) and Thomson et al. (2014) for statistical samples of SMGs.

We derive ALESS067.1 molecular hydrogen mass from the CO (3-2) line luminosity as described in Section 4.1, i.e. $M_{\rm H_2} = (1.7 \pm 0.5) \times 10^{11}$ M$_\odot$, while its dust mass is $M_{\rm dust} \sim 1 \times 10^9$ M$_\odot$ (corrected of a factor 2 following Magdis et al. 2012, Table 1). I note that these values are almost in agreement with other measurements of molecular hydrogen mass (e.g. $M_{H_2} \sim 1.8 \times 10^{11}$ $M_\odot$ by Chen et al. 2017) and dust mass (e.g. $M_{\rm dust} \sim 6 \times 10^8$ $M_\odot$ by da Cunha et al. 2021, that once corrected for dust opacity could be even three times larger, as claimed by the authors). The depletion time-scale is $\tau_{\rm depl} \sim 350$ Myr, in agreement with typical values found in literature for high-z DSFGs (e.g. Casey et al. 2014).

Multiple evidences (such as its X-ray 2−10 keV luminosity, which is $>10^{42}$ erg s^{-1}, and the eventual molecular outflow observed in the B3 ALMA map, mentioned before) suggest a forthcoming quenching of star formation in the host galaxy by the AGN. Even in the case one accepts the merging scenario to describe the CO lines morphology of ALESS067.1, galaxy merger is expected to trigger the central nucleus activity that will eventually quench the star formation in the host galaxy. In order to surely identify (eventual) interactions with minor companions and/or the surrounding ambient and to understand their role and the role of the active nucleus in shaping ALESS067.1 evolution, we need multiwavelength images at higher sensitivity and spatial/spectral resolution. However, even if the clumpy morphology of the galaxy in the optical is actually an evidence of an interacting multiple system, we do not expect the presented picture to be significantly altered, since ALESS067.1 is thought to be by far the dominant object (Targett et al. 2013).

A9 AzTEC.GS25 (J033246.83-275120.9)

AzTEC.GS25 is a DSFG galaxy first detected at 1.1 mm with AzTEC/ASTE ($S_{1.1\,\mathrm{mm}} = 1.9 \pm 0.6$ mJy). For this source, Popesso et al. (2009) report a grism redshift $z_{\mathrm{spec}} = 2.292 \pm 0.001$ (Table 1), based on the detection of rest-frame optical line by the VLT/VIMOS spectroscopy.

We found an ALMA counterpart of the AzTEC source in the DANCING ALMA catalogue by Fujimoto et al. (2017, source ID: 661). We measured a total flux in the ALMA B7 of $S_{1\,\mathrm{mm}} = 5.9 \pm 0.5$ mJy (Table 2), in total accordance with the ALMA Band 7 flux by Cowie et al. (2018), i.e. $S_{850\,\mu\mathrm{m}} = 5.9 \pm 0.18$ mJy (source ID: no. 6; name ALMA033246-275120). Both the millimetre and optical counterparts are resolved and compact. The ALMA radius is $r_{\mathrm{ALMA}} \sim 1.2$ kpc, while the optical radius is slightly larger, i.e. $r_{\mathrm{H}} \sim 1.8$ kpc (Tables 1 and 2). The smooth morphology of ALMA continuum and optical emission of the galaxy suggests that this object must be isolated. These evidences support the scenario in which the bulk of star formation can be traced back to local, *in situ* condensation processes.

AzTEC.GS25 has an X-ray counterpart (IDX 844) in the $\simeq$7 Ms *Chandra* catalogue by Luo et al. (2017). The intrinsic column density $N_{\mathrm{H}} \sim 8.2 \times 10^{22}$ cm^{-2} gives an absorption-corrected intrinsic 2−10 keV luminosity of 6×10^{42} erg s^{-1}. From the analysis of its X-ray emission, Luo et al. (2017) classified the source as AGN (Table 1).

Yun et al. (2012) found a radio (unresolved) counterpart of the AzTEC source in the deep ($\sigma \sim 8$ μJy) VLA 1.4-GHz imaging survey by Kellermann et al. (2008) and Miller et al. (2013). The corresponding radio flux is $S_{1.4\,\mathrm{GHz}} = 89.5 \pm 6.2$ μJy, and it is consistent with the host galaxy star formation activity. The red IRAC/MIPS source associated with radio emission GS25a is located only 6.8 arcsec away from the AzTEC centroid position and Magnelli et al. (2013) assumed it as the NIR counterpart of the millimetre source. The 870-μm LABOCA source LESS J033246.7-275120 (S_870 μm =5.9 ± 0.5 μJy) is well centred on GS25a, and Biggs et al. (2011) also identify the same galaxy as the robust LABOCA counterpart. In Pantoni et al. (2021), we used the flux coming from these multiwavelength counterparts to build the galaxy SED. From the SED analysis, we found AzTEC.GS25 to be a young object (age ∼300 Myr), forming stars at a rate SFR of $\sim$400 M$_\odot$ yr^{-1}, with an sSFR ∼3.8 Gyr^{-1} ($M_\star \sim 8 \times 10^{10}$ M$_\odot$). Gas and dust rich ($M_{\mathrm{gas}} \sim 4 \times 10^{10}$ M$_\odot$; $M_{\mathrm{dust}} \sim 1.4 \times 10^{9}$ M$_\odot$), with a typical depletion time-scale $\tau_{\mathrm{depl}} \sim 100$ Myr, its very intense burst of star formation must trigger a rapid growth of the central AGN.

A10 AzTEC.GS21 (J033247.59-274452.3)

AzTEC.GS21 is a DSFG galaxy at $z_{\mathrm{spec}} = 1.910 \pm 0.001$ [grism redshift by Vanzella et al. 2008, measured with the FORS2 spectrograph (ESO/VLT), ESO/GOODS spectroscopic campaign program in the GOODS-S field]. It was first detected at 1.1 mm with AzTEC/ASTE ($S_{1.1\,\mathrm{mm}} = 2.7^{+0.6}_{-0.7}$ μJy). These photometric data were not included in the SED analysis by Pantoni et al. (2021) since this flux is probably contaminated by other (sub-)millimetre sources in the neighbourhood. Indeed, the H_{160} image of its optical counterpart is disturbed (Fig. 1) and Targett et al. (2013) claim that AzTEC.GS21 is the primary dominant component of a multiple system. The authors measure an effective H_{160} radius of $r_{\mathrm{H}} \sim 2.6$ kpc and a Sérsic index $n_{\mathrm{H}} \simeq 1.3$ (close to a disc-like profile). A more recent analysis on the *HST* image was performed by van der Wel et al. (2012), who find a circularized H_{160} radius $r_{\mathrm{H}} \sim 3.7$ kpc. In this work, we have exploited the latter result.

The source was detected by ALMA in B7 (at $\lambda = 850$ μm) by Cowie et al. (2018), measuring a flux $S_{850\,\mu m} = 3.6 \pm 0.3$ mJy (source ID: no. 20; name ALMA033247-274452). Hatsukade et al. (2018) measured the source flux in the ALMA B6, reporting the value $S_{\mathrm{B6}} = 1.86 \pm 0.32$ mJy. We found a >5-σ continuum detection for this source in the ALMA B9 ($\lambda = 400$−500 μm), measuring a flux $S_{\mathrm{B9}} = 12 \pm 1$ mJy (Table 2). AzTEC.GS21 is not resolved in the ALMA maps. For this reason, we chose the map with the best spatial resolution available in the ALMA archive in order to give at least an upper limit on its size, i.e. $r_{\mathrm{ALMA}} < 0.7$ kpc, which we use to trace the bulk of dusty star formation occurring in the galaxy.

The AzTEC source has a radio (unresolved) counterpart (GS21a) in the deep ($\sigma \sim 8$ μJy) VLA map at 1.4 GHz by Kellermann et al. (2008) and Miller et al. (2013). The corresponding radio flux is $S_{1.4\,\mathrm{GHz}} = 43.6 \pm 6.3$ μJy, which we found to be consistent with the radio emission coming from the host galaxy star formation (Pantoni et al. 2021).

The AzTEC source has an X-ray counterpart (IDX 852) in the catalogue by Luo et al. (2017). The intrinsic absorption column density $N_{\mathrm{H}} \sim 2.27 \times 10^{22}$ cm^{-2} gives an absorption-corrected intrinsic 2−10 keV luminosity of 1.7×10^{42} erg s^{-1}. Luo et al. (2017) classified the source as AGN (Table 1, even if its X-ray luminosity does not clearly emerge from the host galaxy one; Pantoni et al. 2021).

The SED analysis by Pantoni et al. (2021) presents AzTEC.GS21 as a main-sequence galaxy. The galaxy is forming stars at a rate SFR of $\sim$350 M$_\odot$ yr^{-1}, with an sSFR of ∼2 Gyr^{-1}. Massive ($M_\star \sim 2 \times 10^{11}$ M$_\odot$), gas and dust rich ($M_{\mathrm{gas}} \sim 5 \times 10^{10}$ M$_\odot$; $M_{\mathrm{dust}} \sim 6 \times 10^{8}$ M$_\odot$), AzTEC.GS21 is characterized by a depletion time-scale of $\tau_{\mathrm{depl}} \sim 140$ Myr. Notice that its star formation could be fuelled (also) by interactions with some objects in the vicinity, since some works indicate it to be the central, dominant component of a multiple system (Targett et al. 2013). However, the clumpy/disturbed morphology of the source in the optical band may also trace the condensation process of the gas phase towards the centre of the galaxy where the dusty star formation is occurring on a radius of <0.7 kpc. Even accounting the former scenario, we do not expect eventual interactions to have an important impact on the galaxy subsequent evolution, except for prolonging the star formation, since AzTEC.GS21 should dominate by far the gravitational potential of the system (Targett et al. 2013). We expect the galaxy to be quenched by the central AGN in some hundreds of Myr and subsequently become a red and dead galaxy. Clearly, to confirm the right scenario for the evolution of AzTEC.GS21, we need deeper multiwavelength images and at higher resolution.

A11 AzTEC.GS22 (J033212.55-274306.1)

AzTEC.GS22 is a DSFG galaxy first detected at 1.1 mm with AzTEC/ASTE ($S_{1.1\,\mathrm{mm}} = 2.1 \pm 0.6$ mJy). Yun et al. (2012) found a red IRAC/MIPS counterpart for the AzTEC source, with a spectroscopic redshift of $z_{\mathrm{spec}} = 1.794 \pm 0.005$ (table 1 of Wuyts et al. 2009; Targett et al. 2013), which we adopt in this work.

We found a $>5\text{-}\sigma$ continuum detection for AzTEC.GS22 in the ALMA B9 ($\lambda = 400-500$ μm) and we measured a flux $S_{0.45\,\mathrm{mm}} = 5.8 \pm 0.8$ mJy (Table 2), which was essential to constrain the dusty peak of galaxy SED in Pantoni et al. (2021), since the lack of the Herschel 500-μm photometric point. The ALMA source is not resolved in the continuum B9; thus, we provide just an upper limit on its size, i.e. $r_{\mathrm{ALMA}} < 1.7$ kpc, tracing the bulk of dusty star formation.

The most recent analysis of the optical emission of AzTEC.GS22 was performed by van der Wel et al. (2012), who measured an optical size of $r_{\mathrm{H}} \sim 3.2$ kpc, which is more extended than the dust continuum emission (at least of a factor of 2).

The faint radio source GS22a, located 7.8 arcsec away from the AzTEC centroid, is adopted in literature as the most likely counterpart at 1.4 GHz (Yun et al. 2012; Dunlop et al. 2017). Moreover, in Pantoni et al. (2021) we found that the VLA flux at 1.4 GHz ($S_{1.4\,\mathrm{GHz}} = 34.6 \pm 6.5$ μJy) can be traced back solely to galaxy star formation.

From the SED analysis of AzTEC.GS22 (cf. Table 5), we obtain that the object is a main-sequence galaxy. The burst of ongoing star formation in this object is almost 1-Gyr old (age ∼900−1000 Myr) and it is forming stars at a rate of ∼90−100 $\mathrm{M}_{\odot}\,\mathrm{yr}^{-1}$. Massive ($M_{\star} \sim 6 \times 10^{10}\,\mathrm{M}_{\odot}$), gas and dust rich ($M_{\mathrm{gas}} \sim 5 \times 10^{10}\,\mathrm{M}_{\odot}$; $M_{\mathrm{dust}} \sim 1.4 \times 10^{9}\,\mathrm{M}_{\odot}$), AzTEC.GS22 is characterized by a depletion timescale of $\tau_{\mathrm{depl}} \sim 550$ Myr. The huge content of gas and dust could be ascribed simply to its past star formation activity and/or to some kind of interactions (e.g. gas stripping/harassment) with possible companions observed in the optical by Targett et al. (2013). We do not expect these interactions to have a huge impact on the galaxy, since it must dominate the potential well of the multiple system. To confirm this scenario, we need high-resolution multiwavelength imaging. Indeed, the clumpy/disturbed optical morphology, extending over a radius of a few kpcs, could also be interpreted as a signature of the intense dusty star formation of the galaxy.

In the literature, we did not find any X-ray counterpart for the millimetre source, neither in the deep X-ray catalogue by Luo et al. (2017). Since the source lies in a very deep region of the *Chandra* map (equivalent exposure times of $\gtrsim 5$ Ms), we think that the most probable hypothesis to explain the non-detection is that the source is totally obscured in the X-ray. Again, to confirm this interpretation, we need spatially resolved images of the system, at least in the radio and millimetre bands, together with a deeper follow-up in the X-ray.

This paper has been typeset from a TEX/LATEX file prepared by the author.